

We are IntechOpen, the world's leading publisher of Open Access books Built by scientists, for scientists

6,900

Open access books available

185,000

International authors and editors

200M

Downloads

Our authors are among the

154

Countries delivered to

TOP 1%

most cited scientists

12.2%

Contributors from top 500 universities



WEB OF SCIENCE™

Selection of our books indexed in the Book Citation Index
in Web of Science™ Core Collection (BKCI)

Interested in publishing with us?
Contact book.department@intechopen.com

Numbers displayed above are based on latest data collected.
For more information visit www.intechopen.com



Charge Transfer Within Multilayered Films of Gold Nanorods

Mariana Chirea, Carlos M. Pereira and A. Fernando Silva

University of Porto, Faculty of Sciences, Chemistry and Biochemistry Department, Porto, Portugal

1. Introduction

Controlling the charge transport across hybrid nanostructures composed of metal nanoparticles, carbon nanostructures or quantum dots is very important for developing functional sensing, optoelectronic, and photovoltaic devices (Kamat, 2008; Katz & Willner, 2004). The unique electronic, optical, and catalytic properties of metal nanoparticles (1–100 nm), together with the large variety of the synthetic methods available for their synthesis with precise control over the shape and size, provide exciting possibilities for the fabrication of nanoscale assemblies, structures, and devices (Feldheim & Foss Jr, 2004). The self-assembly of nanoparticles into hybrid nanostructures is achieved by using functional molecular linkers which exhibit specific interactions with both the nanoparticles and the substrate. The most stable hybrid nanostructures can be built based on covalent interactions. For example, self-assembled monolayers (SAMs) of aliphatic chain thiols form well defined films on gold surfaces based on spontaneous covalent bonding to the substrate (Love et al., 2005). The charge transfer through these types of molecular linkers is characterized by a decay of the tunnelling current with the length of the linker, the tunnelling coefficient being around $\beta \approx 0.8 \text{ \AA}^{-1}$ (Adams et al., 2003; Finklea, 1987, 1996). However, recent studies demonstrate that the tunnelling decay is not the dominant property of the films when the nanomaterials are tethered at the end of the molecular bridges determining a fast electron transfer process and moreover, this fast electron transfer process is dependent on the size and the shape of the nanomaterials (Bradbury et al., 2008; Chirea et al, 2009, 2010; Kissling et al., 2010). A more detailed research has to be developed in order to fully understand the mechanism behind this fast electron transfer processes taking place at electrodes modified with hybrid nanostructures. Various electrochemical techniques have been used for the investigation of the electron transfer processes taking place at hybrid nanostructured modified electrodes. Cyclic voltammetry, electrochemical impedance spectroscopy, square wave voltammetry, differential pulse voltammetry, potential step chronoamperometry and rotating disk electrodes are among the most used techniques for these electrochemical studies (Chen & Pei, 2001; Chirea et al, 2005, 2007; Hicks et al., 2002, Horswell et al., 2003). Electrochemical impedance spectroscopy (EIS) has been proven as one of the most powerful tools for the investigation of interfacial electrode reaction mechanisms (Katz & Willner, 2003, Yan & Sadik, 2001, Lasia, A. 1999). EIS measures the response (current and its phase) of an electrochemical system to an applied oscillating potential as a function of the frequency. The electrochemical behaviour of redox probes at hybrid nanostructures

modified electrodes is rather complex and depends not only on the nature of the outermost layer but also on the composition of the whole nanostructured film. The EIS technique allows the accurate evaluation of electron transfer kinetics and mass transport despite the complexity of the systems studied (Katz & Willner, 2004 and references therein). In this chapter, it will be presented the fabrication procedure and the electrochemical properties of hybrid nanostructures composed of anisotropic gold nanomaterials, namely gold nanorods (AuNRs) and 1,6hexanedithiol (1,6HDT) which was used as a molecular bridge to covalently bond the rods to the electrodes. The gold nanorods were synthesized based on a seed mediated method using cetyltrimethylammonium bromide as the stabilizing and shape inducing agent (Nikoobakht & El-Sayed, 2003). Control over the size of the gold nanorods was achieved by varying the volume of silver nitrate used during the growth step of these nanomaterials. Multilayered films of gold nanorods and 1,6hexanedithiol were built-up on clean gold electrodes based on the layer-by-layer self-assembly method (Decher & Schlenoff, 2003). Quartz crystal microbalance (QCM), ellipsometry and atomic force microscopy (AFM) measurements were performed in order to determine the self-assembly time of AuNR and 1,6HDT layers, the films' thicknesses, the type of surface bonding of the AuNRs and the films' topographies. The charge transport mechanism through these films was studied as a function of the type of the outermost layer, number of layers within the multilayered films and size of the gold nanorods using $[\text{Fe}(\text{CN})_6]^{3-/4-}$ as redox probes. Cyclic voltammetry, square wave voltammetry and electrochemical impedance spectroscopy were used for the electrochemical characterization of the film modified electrodes. Accurate fittings of the EIS spectra were obtained by using nonlinear square fit software. An excellent agreement between the experimental data and the fitted data has been obtained allowing an accurate correlation of the electrochemical parameters.

2. Experimental section

2.1 Chemicals

Hydrogen tetrachloroaurate (III) trihydrate ($\text{HAuCl}_4 \cdot 3\text{H}_2\text{O}$, 99,999 %, Sigma Aldrich), cetyltrimethyl ammonium bromide ($\text{C}_{19}\text{H}_{42}\text{NBr}$, Sigma, 99%), silver nitrate (AgNO_3 pa quality, Riedel-de Haën), sodium borohydride (NaBH_4 , 96%, Sigma Aldrich), L-ascorbic acid ($\text{C}_6\text{H}_8\text{O}_6$, 99%, Aldrich), 1,6 hexanedithiol ($\text{C}_6\text{H}_{14}\text{S}_2$, Fluka, 97%) methanol (CH_3OH , 99.8%, Sigma), potassium hexacyanoferrate (III), potassium hexacyanoferrate(II) (pa quality, Merck), NaClO_4 (pa quality, Merck), HClO_4 (70%, redistilled, 99.999%, Aldrich), H_2O_2 30% (Fluka), H_2SO_4 (pure, Pronalab) were used as received. Millipore filtered water (resistivity > 18 $\text{M}\Omega \text{ cm}$) was used to prepare all aqueous solutions and for rinsing. Prior use, all the glassware were cleaned with freshly prepared *aqua regia* (HNO_3 : HCl =1:3, % v/v), rinsed abundantly with Millipore water and dried.

2.2 Synthesis of 2.44 and 3.48 aspect ratios gold nanorods

The gold nanorods were prepared following the procedure published in the literature (Nikoobakht, & El-Sayed, 2003). First, spherical gold nanoparticles were synthesized by reducing HAuCl_4 (aqueous solution of 5.0 mL, 0.00050M) with ice-cold NaBH_4 solution (0.60 mL, 0.01M) under strong stirring in the presence of cetyltrimethylammonium bromide (5 mL aqueous solution, 0.20 M). The resulted seeds were kept for 2 hours at 25°C. Consecutively,

growth solutions were prepared by adding ascorbic acid (70 μL of 0.0788 M) into two solution mixtures composed of cetyltrimethylammonium bromide aqueous solution (5 mL, 0.20 M), 0.050 or 0.15 mL of AgNO_3 solution (0.0040 M) respectively, and HAuCl_4 (5.0 mL of 0.0010 M). To these mixtures 12 μL of the prepared seed solution were added at 30°C solution temperature, which determined the growth of the nanorods proved by the apparition of the specific colour for each sample within 10 minutes. The short rods featured a blue colour in aqueous solution whereas the large rods featured a pink-brownish colour (Figure 1a and 1d). The gold nanorods were purified by washing with Millipore water, centrifugation and decantation. This procedure of purification was performed twice.

2.3 Transmission electron microscopy measurements

A drop of each rod solution was cast on formvar copper carbon grids, let to dry for at least 24 hours and imaged. The TEM images were recorded using a transmission electron microscope Hitachi 8100 equipped with a Rontec Standard EDS detector and digital images acquisition, operating at 200 kV and having a point resolution of 1.6 nm. The length/width ratio of the rods was evaluated using Image J software.

2.4 UV-Vis spectroscopy measurements

The optical spectra of the AuNRs samples were recorded on a Hitachi U-3000 spectrophotometer in the range 200-900 nm, using quartz cuvettes with 1cm light path and freshly prepared Au NRs solutions.

2.5 Fabrication of 1,6hexanedithiol/gold nanorod multilayers

2.5.1 Quartz Crystal Microbalance measurements

The QCM measurements were performed with a QCM-Z500 apparatus (KSV, Finland) which can monitor ΔF changes for six overtone frequencies (5, 15, 25, 35, 45 and 55MHz). The QCM electrodes (gold coated quartz crystals, 0.785 cm^2 area) were washed with freshly prepared Piranha solution (3:1 mixture of concentrated sulphuric acid and hydrogen peroxide, 30%, *Caution! Piranha solution is corrosive and reacts violently with organic materials*) rinsed with large amounts of Millipore water, dried in a stream of nitrogen and placed in the QCM cell for surface modification. The base line was recorded in the presence of ethanol. Consecutively, the pure solvent was gently removed from the QCM cell and an ethanolic solution of 1,6 hexanedithiol (15 mM) was injected into the cell. The frequency change was recorded continuously during the adsorption process of the dithiol, at 25 °C solution temperature (results not shown). Consecutively, the SAM modified QCM electrode were washed with ethanol and Millipore water, dried in a stream of nitrogen and analyzed by tapping mode atomic force microscopy (AFM). After AFM imaging the 1,6HDT modified QCM electrode was reinserted in the QCM chamber and a second base line was recorded for 20 minute using Millipore water as the solvent. The Au-1,6HDT modified electrode was further modified with gold nanorods by gentle injection of freshly prepared AuNR₁ solution (0.50 mg/mL) at a solution temperature of 35°C. The resulted Au-1,6HDT-AuNR₁ modified electrode was removed from the QCM cell, washed persistently with Millipore water, dried in a stream of nitrogen and imaged by tapping mode AFM. The Au-1,6HDT-AuNR₁ modified electrode was reinserted in the QCM cell and a third layer, (a 1,6HDT layer) was

self-assembled from ethanolic solution. These steps were repeated until a number of 8 layers were built-up on the QCM electrode. The same procedure was followed for the build-up of multilayers containing hexanedithiol and large gold nanorods (AuNR₂, 0.50mg/mL). The resulted QCM-multilayer modified electrodes were analyzed by atomic force microscopy. The QCM measurements were performed in order to estimate the necessary self-assembly time for each layer.

2.5.2 Atomic force microscopy measurements

The resulted 1,6HDT/AuNR multilayer modified QCM electrodes were imaged in air using a Molecular Imaging PicoLe AFM in tapping mode and Silicon cantilevers (Nanosensors) with a resonance frequency of 200-400 kHz. Topographic, amplitude and phase images were recorded for all the samples with a resolution of 512×512 pixels.

2.5.3 Ellipsometry measurements

The thickness of the multilayers was determined using a Multi-Wavelength Discrete Ellipsometer. First, the Brewster angle was determined for the bare gold QCM electrode previously washed with Piranha solution, large amounts of Millipore water and dried in a stream of nitrogen. The search of the Brewster angle was performed for several angles of the ellipsometer: 74°, 70°, 69°, 68° and the best results were obtained for the angle of 68°. The refraction index (n) and the extinction coefficient (K) determined for the bare gold QCM were $n = 0.496 \pm 0.011$ and $K = 2.323 \pm 0.006$. These parameters values were used for the determination of the multilayers' thicknesses.

2.5.4 Electrochemical measurements

Cyclic, square wave voltammetry and electrochemical impedance spectroscopy measurements were performed on a PGSTAT 302N potentiostat (EcoChemie B.V., The Netherlands) for each new layer self-assembled on the working electrodes. All electrochemical experiments were carried out in a conventional three-electrode cell equipped with a working electrode of gold (with an area of 0.0314 cm²), a Pt wire as the counter electrode and an Ag/AgCl (3M KCl) electrode as the reference electrode. The electrochemical cell was placed in a Faraday cage in order to minimize the electrical noise. The gold electrodes were cleaned as previously explained (Chirea et al, 2005) and consecutively modified following the procedure used for the QCM experiments. The electrolyte solution consisted of 0.0005M [Fe(CN)₆]^{3-/4-} and 0.1NaClO₄. Cyclic voltammograms were measured between -0.2 and 0.6 V at several scan rates (25, 50, 75, 100mV/s) for each layer self-assembled on the gold electrodes. The square-wave voltammograms were measured for the same potential window, at frequency varying between 10Hz to 75Hz, using 50mV amplitude and a step potential of 2mV. Electrochemical impedance spectroscopy (EIS) measurements were performed for a frequency range of 10000 to 0.1 Hz and amplitude of 20 mV at the formal potential of the [Fe(CN)₆]^{3-/4-} redox couple (0.210V vs. Ag/AgCl (KCl, 3M). Before each measurement, N₂ was purged into the solution for 15 minutes for deaeration. The electrochemical measurements were performed twice on freshly modified electrodes and similar results were obtained.

3. Results and discussions

3.1 Characterization of gold nanorods

It has been demonstrated that the growth of gold nanorods in aqueous solution from spherical gold nanoparticles (4nm average diameters) in the presence of cetyltrimethyl ammonium bromide takes place simultaneously on all directions until the seeds are reaching a critical size allowing surfactant binding (Nikoobakht & El-Sayed, 2003).

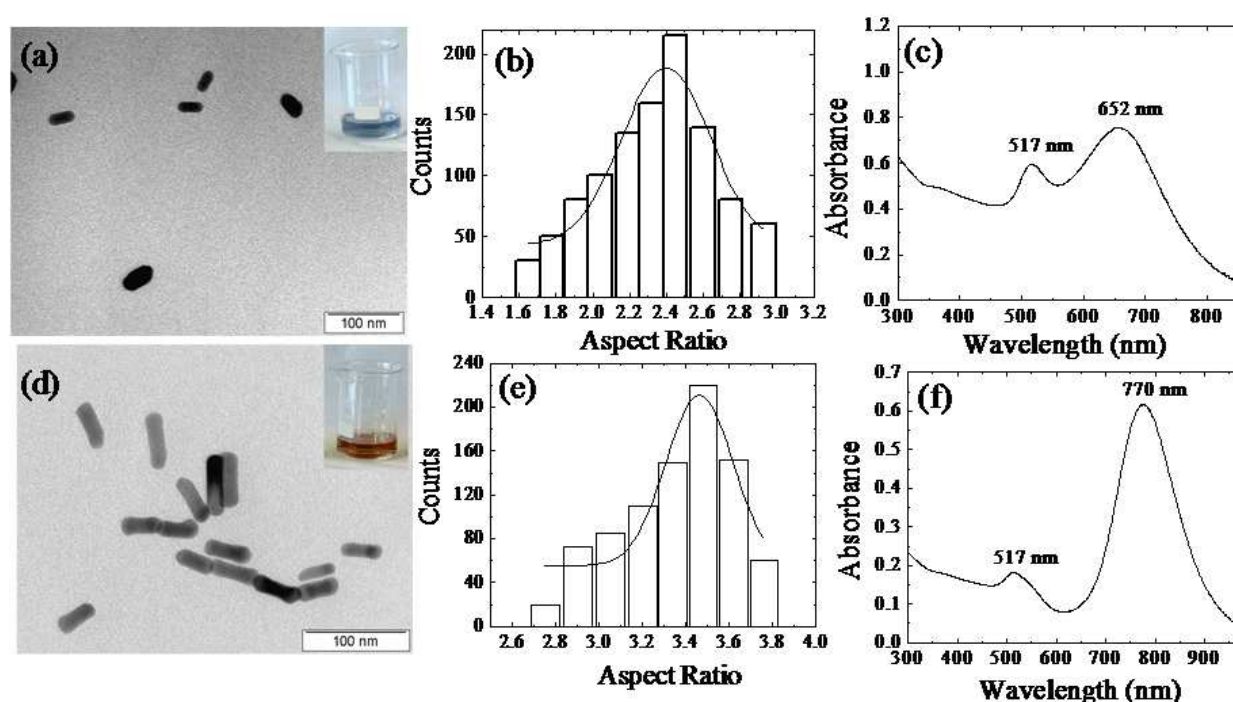


Fig. 1. Transmission electron microscopy images, size distribution histograms, and UV-Vis spectra of 2.44 aspect ratio gold nanorods (a, b, c) and 3.48 aspect ratio gold nanorods (d, e, f). Insets of a and d : digital images of the gold nanorods solutions.

Moreover, the growth in the longitudinal direction takes place parallel to the $\{001\}$ planes, which is accompanied by formation of four relatively unstable $\{110\}$ facets and four $\{111\}$ facets. The surfactant has a stronger affinity to $\{110\}$ facets determining a slower growth on the width of the rods than on the longitudinal direction characterized mainly by $\{111\}$ facets. The growth rate on different facets determines the final shape of these nanomaterials. The presence of Ag ions in the growth solution (from AgNO_3 used as growth agent) generates Ag-Br pairs between the headgroups of the capping material. These Ag-Br pairs may decrease the charge density on the bromide ions determining less repulsion between the neighbouring headgroups on the rods surface and as a result controlling the size of the rods. This seed-mediated method allows control over the size of the rods by varying the AgNO_3 volume, at high concentration of surfactant. In accordance, two different sized gold nanorod samples were synthesized following this method. The morphology (size, shape) and the optical properties of the gold nanorods were analyzed by transmission electron microscopy and UV-Vis spectroscopy (Figure 1). An accurate size distribution was estimated based on TEM images. The gold nanorods were 2.44 aspect ratio (AuNR_1 , 35.48 nm length per 14.52

nm width, Figure 1a and 1b) and 3.48 aspect ratio (AuNR₂, 51.56 nm length per 14.80 nm width, Figure 1d and 1e). Transverse plasmon bands at 517 nm and longitudinal plasmon bands at 652 nm (Figure 1c, AuNR₁, blue colour) or 770 nm (Figure 1f, AuNR₂, pink-brownish colour) were observed in the optical spectra of the rods demonstrating an evident increase of rods size with increased volumes of AgNO₃ added during the growth procedure (see section 2.2).

3.2 Characterization of 1,6hexanedithiol/gold nanorod multilayers by quartz crystal microbalance, ellipsometry and atomic force microscopy

In the following discussion n denotes the number of layers self-assembled on the QCM gold electrodes. The bare gold corresponds to $n = 0$, the 1,6hexanedithiol layers correspond to n odd ($n = 1, 3, 5, 7$) whereas the gold nanorods layers correspond to n even ($n = 2, 4, 6, 8$). In accordance, the first bilayer corresponds to $n = 2$, the second bilayer corresponds to $n = 4$, the third bilayer corresponds to $n = 6$ whereas the forth bilayer corresponds to $n = 8$. The 1,6HDT layers were self-assembled on the QCM gold electrodes from ethanolic solution at 25°C whereas the consecutive AuNRs layers were self-assembled from aqueous solution at 35°C. As determined previously, (Chirea et al., 2010) these are the adequate self-assembly condition in order to obtain dense and vertically aligned gold nanorods using 1,6hexanedithiol as a bridge molecule. The self-assembly time for each layer was determined by QCM measurements. The first hexanedithiol layer ($n = 1$) was self-assembled after 14 hours whereas the consecutive gold nanorod layer ($n = 2$), was self-assembled after 7 hour in the case of short rods or 15 hours in the case of large rods at a solution temperature of 35°C (Chirea, 2010). For the multilayer containing short rods (AuNR₁, 2.44 aspect ratio), the third layer self-assembled on the modified electrodes, a 1,6HDT layer ($n = 3$) was formed after 16 hours, the consecutive AuNR₁ layer ($n = 4$) was self-assembled after 10 hours, the 5th layer, a 1,6HDT layer, was self-assembled after 19 hours, the consecutive AuNR₁ layer was self-assembled after 12 hours ($n = 6$), whereas the last two layers were self-assembled after 19 hours ($n = 7$) and 15 hours ($n = 8$). The multilayer containing 3.48 aspect ratio gold nanorods was build-up for the self-assembly times of 14 hours ($n = 1$), 15 hours ($n = 2$), 11 hours ($n = 3$), 16 hours ($n = 4$), 18 hours ($n = 5$), 18 hours ($n = 6$), 15 hours ($n = 7$) and 6 hours ($n = 8$) respectively. The deposited mass has decreased with increasing number of layers self-assembled on the gold electrodes (results not shown). This decrease of deposited mass with each new layer self-assembled on the Au-QCM electrodes suggests a pyramidal growth of the multilayers. For example, the highest number of small gold nanorods was self-assembled on the first 1,6hexanedithiol monolayer formed on the Au-QCM electrodes which is a well organized film. The tapping mode AFM image of this bilayer illustrates a vertical alignment of the rods to the substrate surface (Figure 2a, $n = 2$, AuNR₁, 35.48 nm length per 14.52 nm width). The third layer self-assembled on the modified QCM electrode, a 1,6hexanedithiol layer ($n = 3$) determined no evident change in topography (results not shown).

Based on the strong affinity of thiols toward covalent bonding to gold surfaces (Love et al., 2005), it is expected that the 1,6HDT layer ($n = 3$) will cover the rods removing the cetyltrimetyl ammonium bromide from their surface through a place exchange reaction (Hostetler, M. J. et.al, 1999), and possibly will connect them on a horizontal plane if they are in very close vicinity. However, the chemical bonding of the rods on a horizontal plane may change or not the films topographies. The consecutive self-assembly of a fourth layer, namely an AuNR₁ layer, (Figure 2b, $n = 4$) has generated a similar film topography

(vertically aligned nanorods) with a lower surface coverage of rods than the previous AuNR₁ layer (Figure 2a, $n = 2$). It seems that the only possibility to connect gold nanorods on an upper layer ($n = 4$) is at the ends of the gold nanorods from the previous layer ($n = 2$) through the 1,6hexanedithiol molecules acting as molecular bridges ($n = 3$). In consequence, the number of 1,6hexanedithiol molecules available for further chemical interactions are the molecules at the ends of each vertically aligned rod from a previous layer which implies already a lower number of 1,6HDT molecules than in the $n = 1$ layer. This chemical structure has determined a pyramidal growth of the multilayered film (Figure 2). Moreover, the AFM images have revealed the presence of neighbour rods within the same layer (the thicker “rods” features) together with a decreasing surface coverage of the gold nanorods in the upper layers of the multilayered film (Figure 2b, c, d). The sequential self-assembly of AuNR₁ and 1, 6 hexanedithiol layers up to a maximum 8 layers have generated similar topographies (Figure 2c, d). The surface roughness has increased with the numbers of bilayers self-assembled on the electrodes from 12.24 nm (Figure 2a, $n = 2$), to 15.36 nm (Figure 2b, $n = 4$), to 18.55 nm (Figure 2c, $n = 6$) and to 20.20 nm (Figure 2d, $n = 8$). The increase of surface roughness proves a progressive growth of the film upon self-assembly of each (1,6HDT/AuNR₁) bilayer. The AFM analysis of the film confirms its pyramidal growth with decreasing surface coverage of gold nanorods within consecutive layers (Figure 2). The tapping mode AFM analysis of the multilayer film containing layers of 1,6hexanedithiol and large rods (AuNR₂, 51.56 nm/14.80 nm average sizes) is illustrated in Figure 3.

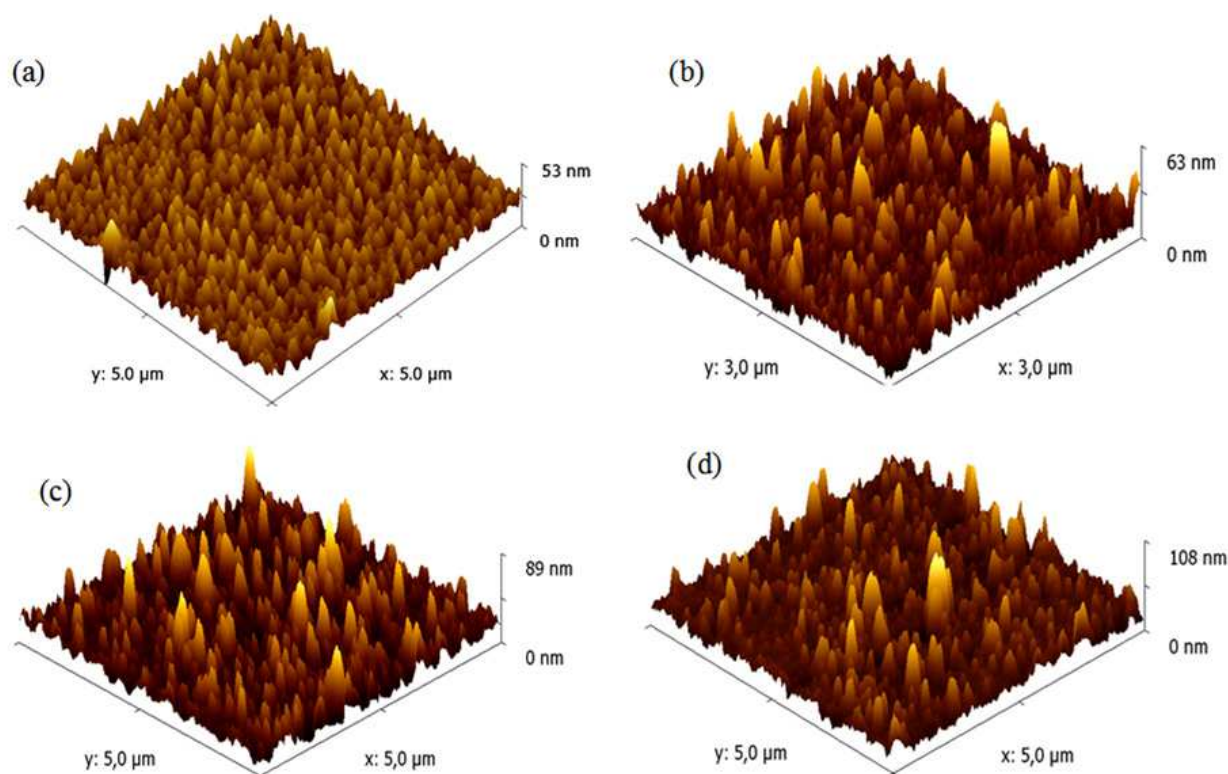


Fig. 2. Tapping mode atomic force microscopy images of Au-(1,6HDT-AuNR₁)₄ multilayers showing the progressive build-up of the film: (a) first bilayer, ($n = 2$), (b) second bilayer, ($n = 4$), (c) third bilayer ($n = 6$), and (d) fourth bilayer ($n = 8$). AuNR₁ were 35.48nm/14.52nm average sizes.

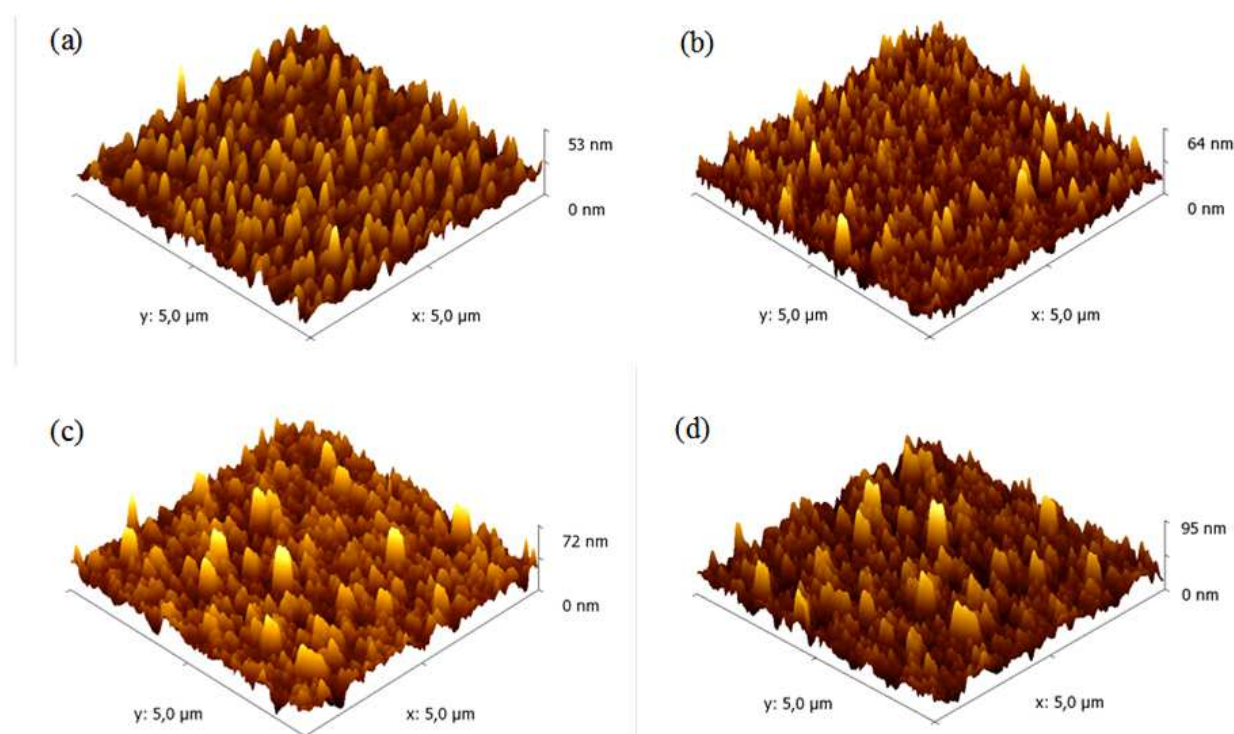


Fig. 3. Tapping mode atomic force microscopy images of Au-(1,6HDT-AuNR₂)₄ multilayers showing the progressive build-up of the film: (a) first bilayer, ($n = 2$), (b) second bilayer, ($n = 4$), (c) third bilayer ($n = 6$), and (d) fourth bilayer ($n = 8$). AuNR₂ were 51.56 nm/14.80 nm average sizes.

The topographic features of this film suggest that the AuNR₂ were attached vertically at the ends of the rods from the previous layer with a decreased surface coverage (compare Figure 3b and 3a). The consecutive self-assembly of 1,6hexanedithiol and AuNR₂ layers (Figure 3c, $n = 6$) has generated a more dense structure implying a covalent bonding of the large rods both at the tips of the previous AuNR₂ layer ($n = 4$) and, in higher number, in-between the rods of the same $n = 4$ layer. A similar dense surface coverage was observed after the self-assembly of the next 1,6hexanedithiol/AuNR₂ bilayer (Figure 3d, $n = 8$). The surface roughness increased progressively with increasing number of bilayers from 14.26 nm (Figure 3a, $n = 2$), to 18.23 nm (Figure 3b, $n = 4$), to 24.20 nm (Figure 3c, $n = 6$) and to 28.0 nm (Figure 3d, $n = 8$), respectively. The progressive increase of surface roughness demonstrates also a progressive increase of film thickness. If the gold nanorods within a layer are in very close vicinity, then the 1,6hexanedithiol is connecting them on a horizontal plane generating quit ordered features with twin nanorods as illustrated in Figure 4. The topographic analysis of both types of films demonstrates that the film growth and film density depend on the size of the gold nanorods. The short rods tend to organize themselves within quit homogeneous films being covalently bonded at their ends through the 1,6hexanedithiol molecular bridges and generating a well organized network.

Contrarily, the large rods tend to fill-up first the free spaces in-between the rods in a previous layer and to covalently bond in an upper layer only with a low surface coverage. The different chemical structures of these two types of multilayers will determine a different electrochemical behaviour as it will demonstrate in the following paragraphs. The vertical

alignment of the rods within these films is in accordance with previous observation related to the type of surface bonding (end-bonding) of the rods when self-assembled on gold electrodes at 35°C solution temperature and using the 1,6hexanedithiol as bridge molecules (Chirea et al., 2009, 2010). The thicknesses of the multilayers were determined by ellipsometry measurements. The average thickness of Au-(1, 6HDT-AuNR₁)₄ multilayered film was $188, 85 \pm 1.05$ nm yielding a refraction index of 2.78 ± 0.11 and an extinction coefficient of $K = 3.42 \pm 0.03$ whereas the average thickness of the Au-(1, 6HDT-AuNR₂)₄ multilayered film was $227, 10 \pm 1.2$ nm yielding a refraction index of $n = 3.70 \pm 0.15$ and a extinction coefficient of $K = 3.93 \pm 0.05$. The estimated film thicknesses are in accordance with a vertical alignment of the nanorods to the substrate surface as demonstrated also by AFM measurements (Figure 2, 3 and 4).

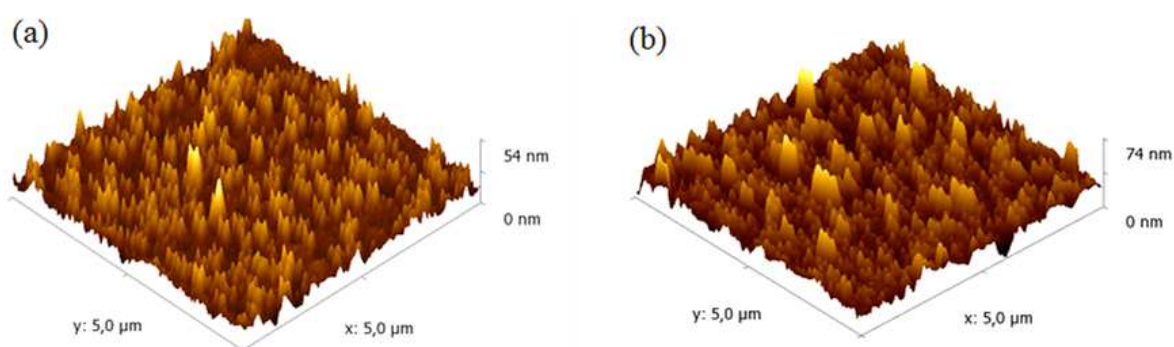


Fig. 4. Tapping mode atomic force microscopy images of the multilayered film illustrating the effect of the 1,6HDT monolayer as the outermost layer on the overall film topography: (a) Au-1,6HDT-AuNR₂-1,6HDT film ($n=3$), (b) Au-1,6HDT-AuNR₂-1,6HDT-AuNR₂-1,6HDT-AuNR₂-1,6HDT film ($n=7$). The surface roughness was 7.47 nm (a) and 15.32 nm (b).

3.3 Electrochemical characterization of 1,6hexanedithiol/gold nanorod multilayers

As previously mentioned n denotes the number of layers self-assembled on the gold electrodes. The bare gold corresponds to $n=0$, the 1,6hexanedithiol layers correspond to n odd ($n=1, 3, 5, 7$) whereas the gold nanorods layers correspond to n even ($n=2, 4, 6, 8$). The electrochemical properties of the 1,6hexanedithiol/gold nanorod multilayers were studied as a function of the number of layers self-assembled on the gold electrodes and as a function of the sizes of the gold nanorods. The electrolyte consisted of 0.0005M K₃[Fe(CN)₆]³⁻ and 0.0005M K₄[Fe(CN)₆]⁴⁻ (0.0005M) dissolved in 0.1M NaClO₄ aqueous solution. Cyclic and square wave voltammetry measurements as well as electrochemical impedance spectroscopy measurements were performed for each layer self-assembled on the gold electrodes in order to elucidate the electron transfer process taking place at the 1,6hexanedithiol/gold nanorod modified electrodes.

3.3.1 Electrochemical characterization of multilayers containing short gold nanorods

Figure 5 shows the cyclic (Figure 5a and 5b) and square wave voltammograms (Figure 5c and 5d) recorded at the Au-(1,6HDT-AuNR₁)₄ multilayer modified gold electrodes in aqueous solution of 0.1M NaClO₄ and 0.0005M [Fe(CN)₆]^{3-/4-}. As mentioned previously, the average sizes of the rods incorporated into this film were 35.48 nm lengths per 14.52 nm

width (AuNR₁, Figure 1a, b) with an aspect ratio of 2.44. The gold nanorods were self-assembled in end-bonding topography through 1,6hexanedithiol bridges generating a quit homogeneous film (Figure 2). The electrical properties of this film were highly dependent on the type of outermost layer. The Faradaic process was highly hindered by the 1,6hexanedithiol layers (Figure 5, $n = 1, 3, 5, 7$). This electrochemical behaviour is caused by the insulating properties of this dithiol when self-assembled on gold electrodes (Chirea et al., 2009, 2010; Chou et al., 2009). For example, the first layer self-assembled on the gold electrodes determined a disappearance of the Faradaic currents in the cyclic and square wave voltammograms (Figure 5, $n = 1$, black curve) as compared to the bare gold electrode (Figure 5, $n=0$, dashed black curve) illustrating a dense packing of the 1,6hexanedithiol layer on the gold electrodes. In other words, the 1,6hexanedithiol is blocking the electronic communication between the $[\text{Fe}(\text{CN})_6]^{4-/3-}$ in solution and the underlying bare gold electrode. The consecutive self-assembly of an AuNR₁ layer determined the reappearance of the Faradic currents in the cyclic and square wave voltammograms (Figure 5a, c, $n = 2$, red curve) generating a quasi reversible behaviour of the $[\text{Fe}(\text{CN})_6]^{3-/4-}$ redox couple. The third layer self-assembled on the modified electrodes (a 1,6HDT layer) has determined a drastic decrease of peak currents in the cyclic and square wave voltammograms (Figure 5b, d, $n = 3$, purple curve), again due to its insulating properties confirming a high coverage with 1,6HDT molecules on AuNR₁ surfaces from the previous layer. Nevertheless, the presence of the small gold nanorods in the inner layer ($n = 2$) seems to facilitate the electron transfer process despite the complete electronic blocking generated by the 1,6hexanedithiol layers ($n = 1$ and $n = 3$). At this stage of the multilayer build-up, the electron transfer process is based on electron tunnelling through the dithiol layers (very low peak currents ($n = 3$) or no peak currents ($n = 1$) in the CVs and SQWVs, Figure 5) and electron transport mediated by the gold nanorods from the inner layer ($n = 2$). A similar electrochemical behaviour has been observed at citrate stabilized gold nanoparticle/1,4 benzenedimethanethiol multilayers modified gold electrodes. Abdelrahman et al. have shown that these gold nanoparticles have a good catalytic activity toward $[\text{Ru}(\text{NH}_3)_6]^{3+}$ in solution, despite the electronic blocking induced by the 1,4 benzenedimethanethiol layers used to connect the gold nanoparticles into dense films. Moreover these gold nanoparticle/1,4 benzenedimethanethiol multilayers have proven also highly efficient for oxygen reduction (Abdelrahman et al., 2006).

In the present work, the self-assembly of a fourth layer, a AuNR₁ layer, re-established an efficient electron transfer process depicted through high peak currents in the CVs and SQWVs (Figure 5a, c, $n = 4$, green curve) demonstrating also a high catalytic activity of these rods. These electrical features demonstrate a stepped electron transfer process consisting of : (i) increase of the interfacial concentration of the negatively charged redox probes at the positively charge gold nanorods surfaces by electrostatic attraction (ii) electron transport mediated by the gold nanorods and (iii) and coherent electron tunnelling through the 1,6hexanedithiol layers toward the underlying bare gold electrode (Scheme 1). A remarkable feature is to be mentioned: the Faradaic currents are slightly lower at the four layers modified electrode than at the two layers modified electrode (in Figure 5 a, c compare $n = 2$ and $n = 4$) but both films determined a faster electron transfer than at the bare gold electrode (higher Faradaic currents in SQWVs than at the bare gold, see Figure 5c). This electrochemical behaviour is caused by two features: (i) high catalytic activity of the short rods which is nullifying the electronic blocking induced by the 1,6hexanedithiol layers

assuring an coherent electron tunnelling through these molecular bridges and (ii) the surface coverage with gold nanorods is decreasing as shown by AFM imaging (compare Figure 2a and Figure 2b).

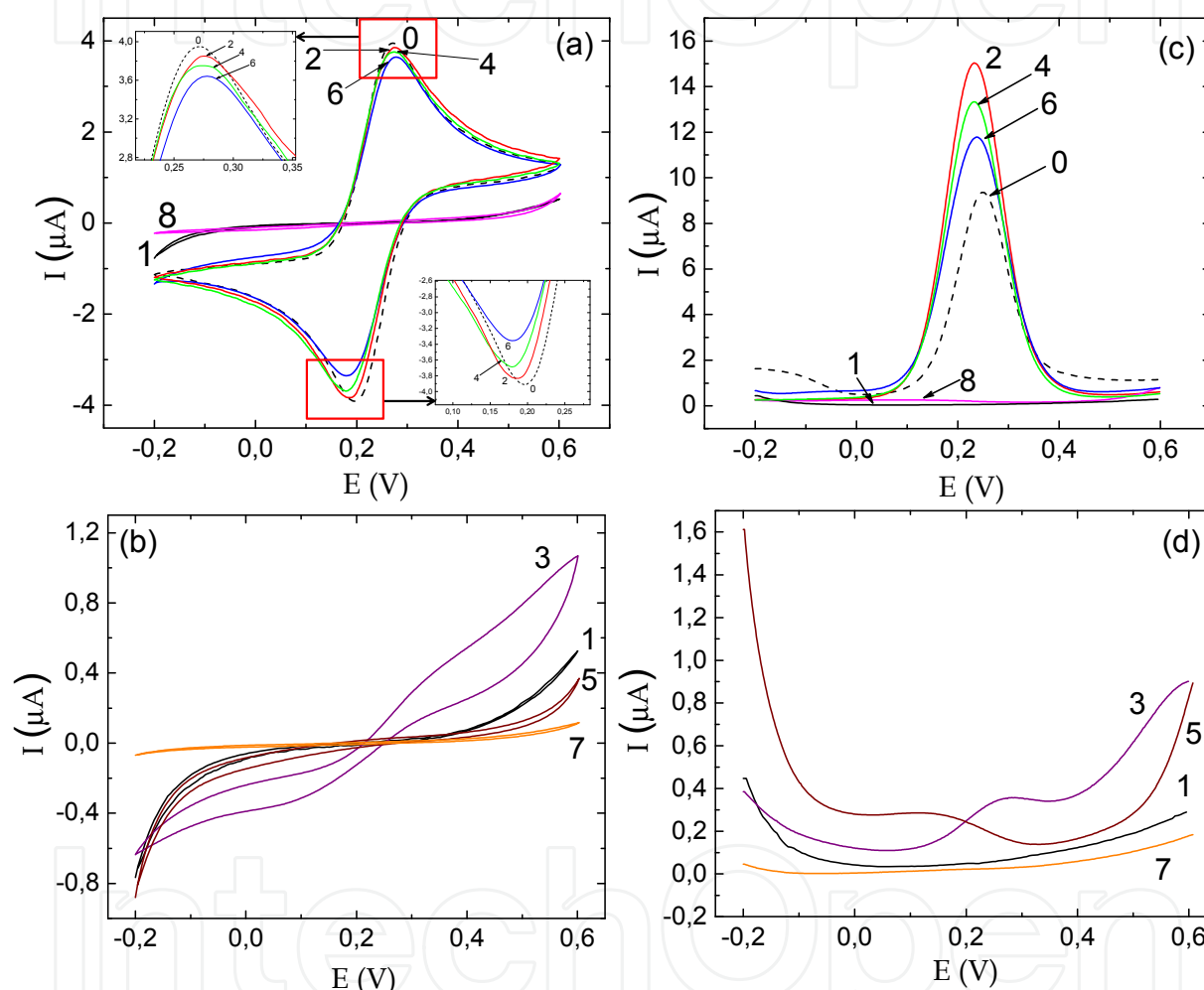
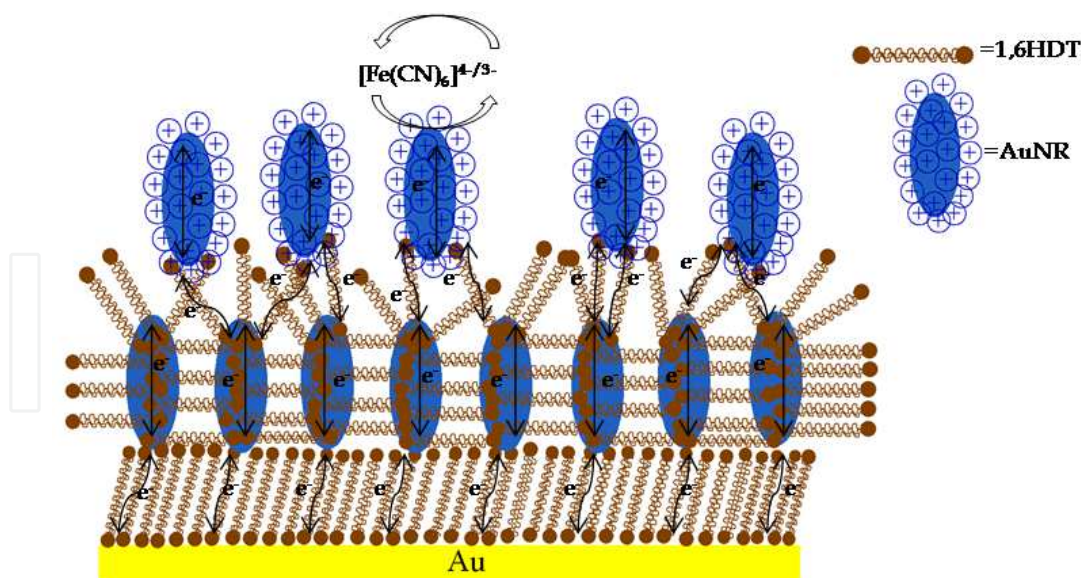


Fig. 5. Cyclic voltammograms (a, b) and square wave voltammograms (c, d) recorded at the Au-(1, 6HDT-AuNR₁)₄ multilayer modified gold electrodes in aqueous solution of 0.1M NaClO₄ and 0.0005M [Fe(CN)₆]^{3-/4-}: bare gold ($n = 0$), 1,6HDT outermost layers ($n = 1,3,5,7$) and AuNR₁ outermost layers ($n = 2,4,6,8$), respectively.



Scheme 1. Schematic representation of the electron transfer process at 1,6hexanedithiol/gold nanorods multilayers modified electrode.

The sequential self-assembly of the fifth layer, a 1,6hexanedithiol layer, determined a complete electronic blocking between the redox probes in solution and the underlying bare gold electrode depicted through the disappearance of the Faradaic current in the CV (Figure 5b, $n = 5$, wine curve) or a drastic decrease of Faradaic current in the SQWV (Figure 5d, $n = 5$, wine curve) and shifting of the peak current toward less positive potentials. This difference of the electrochemical features in the cyclic and square wave voltammograms for the same layer is due to the difference of electrochemical sensitivity between the two techniques. Square wave voltammetry has as main advantage the discrimination of the non-Faradaic (capacitive) currents which is achieved by measuring the current at the end of the imposed square-wave pulse. In this way the ratio between the Faradaic and non-Faradaic currents is very high because almost no capacitive currents are measured at the end of the measuring time. This cannot be achieved by cyclic voltammetry. The square wave signal consists of a symmetrical square wave pulse superimposed on a staircase waveform (Mirčeski et al.2007) which assures a higher sensitivity of this technique toward surface confined electron transfer processes than the cyclic voltammetry. In consequence, the square wave voltammograms illustrate more accurate the effect of each layer self-assembled on the gold electrodes. The sixth layer self-assembled on the gold electrodes, an AuNR₁ layer, restored the efficient electronic communication between the redox probes in solution and the underlying bare gold electrode generating cyclic and square wave voltammograms with well defined peak currents and diminished peak separations (Figure 5a, b $n = 6$, blue curve). The 7th layer self-assembled on the gold electrodes (Figure 5, $n = 7$, orange curve) showed a similar electrochemical behaviour as the previous dithiol layers, namely an insulating effect, whereas the 8th layer determined no evident increase of Faradaic current (Figure 5a,c, $n = 8$, pink curve). At this stage of the multilayer build-up the low surface density of the rods does not allow a further improvement of the overall electron transfer process. The peak currents and the peak-to-peak separations in the cyclic voltammograms varied as follows: $I_a = 3.95\mu\text{A}$, $\Delta E_p = 0.071\text{V}$, for $n = 0$ (bare gold electrode), $I_a = 3.85\mu\text{A}$, $\Delta E_p = 0.091\text{V}$, for $n = 2$,

(Au-1,6HDT-AuNR₁), $I_a = 0.58 \mu\text{A}$, $\Delta E_p = 0.369\text{V}$, for $n = 3$, (Au-1,6HDT-AuNR₁-1,6HDT), $I_a = 3.75 \mu\text{A}$, $\Delta E_p = 0.095\text{V}$, for $n = 4$, (Au-1,6HDT-AuNR₁)₂, $I_a = 3.64 \mu\text{A}$, $\Delta E_p = 0.097\text{V}$, for $n = 6$, (Au-1,6HDT-AuNR₁)₃ whereas for the other layers ($n = 1, 5, 7$ and 8) there were no peak currents in the CVs (Figure 5a,b). As proven by these parameters value, the current densities in the CVs are decreasing with the number of AuNR₁ present in each layer. As seen by AFM analysis, the number of gold nanorods in direct contact with the electroactive species from solution is decreasing within each new layer self-assembled on the gold electrodes (Figures 2). Due to their high surface to volume ratio, the gold nanorods act as nanoelectrodes proving a strong catalytic effect in the overall electrochemical process. If their number decreases then the current generated at these nanoelectrodes is decreasing. In consequence the surface density of the rods has a strong influence on the overall electrochemical process. In the square wave voltammograms, the lowest peak current was recorded at the film containing all 8 layers ($n = 8$, Figure 5c), for which the number of AuNR₁ covalently bonded to the modified electrode is the smallest (Figure 3d) and the distance from the underlying bare gold surface is the longest. The corresponding peak currents and shifting of the peak potentials in the square wave voltammograms varied as follows: $I_a = 9.40 \mu\text{A}$ at 0.247V for $n = 0$, $I_a = 15.04 \mu\text{A}$ at 0.233V for $n = 2$, $I_a = 0.35 \mu\text{A}$ at 0.274V for $n = 3$, $I_a = 13.37 \mu\text{A}$ at 0.232V for $n = 4$, $I_a = 0.28 \mu\text{A}$ at 0.142V for $n = 5$, $I_a = 11.72 \mu\text{A}$ at 0.236V for $n = 6$, $I_a = 0.32 \mu\text{A}$ at 0.065V for $n = 8$ (Figures 5c and 5d). For the 1,6hexanedithiol outermost layers having an insulating effect, the redox current at any potential is given by the expression (Xu et al., 1993):

$$I = I_0 e^{-\beta d} \quad (1)$$

where I_0 is the current measured at the bare electrode, β is the potential independent electron tunnelling coefficient, and d is the thickness of the monolayer. For an electrochemical reaction at equilibrium, using equation (1) it can be obtained:

$$k = k_0 e^{-\beta d} \quad (2)$$

where k_0 and k are the electron transfer rate constants at the bare and 1,6HDT-SAM modified electrode. The heterogeneous electron-transfer rate constant (k_{et}) at the modified electrodes can be calculated using equation (3) (Chirea et al, 2007 and references therein):

$$k_{et} = (RT) / (n^2 F^2 A R_{CT} c^0) \quad (3)$$

where R is the gas constant, T is temperature (K), F is the Faraday constant, A is the electrode area (0.0314 cm^2), R_{CT} is the charge-transfer resistance, c^0 is the concentration of the redox couple in the bulk of solution ($0.5 \times 10^{-3} \text{ mol/cm}^3$) and n is the number of transferred electrons per molecule of the redox probe ($n = 1$ for the $[\text{Fe}(\text{CN})_6]^{3-/4-}$ probes). From the fittings of the impedance spectra (Figures 6, 7), it was obtained the apparent charge transfer resistance, R_{CT} , for each layer self-assembled on the gold electrodes (table 2). The heterogeneous electron-transfer rate constants, k_{et} , for each layer self-assembled on the gold electrode were estimated using R_{CT} parameters and based on equation (3), (table 1). The variation of the heterogeneous electron-transfer rate constant, k_{et} , shows a three order magnitude increase upon the self-assembly of the first AuNR₁ layer ($k_{et} = 1.63 \times 10^{-5} \text{ cm} \times \text{s}^{-1}$

$n=2$, table 1) as compared to the first 1,6HDT-SAM ($k_{et} = 0.48 \times 10^{-8} \text{ cm} \times \text{s}^{-1}$, $n = 1$, table1). The consecutive self-assembly of a 1,6HDT layer ($n = 3$, table 1) determined two orders magnitude decrease of the k_{et} , followed by a two orders magnitude increase of the k_{et} for the next AuNR₁ self-assembled layer ($n = 4$, table1). This oscillation of the k_{et} is repeated up to the 7th layer. For the last layer self-assembled on the multilayer modified electrodes ($n = 8$, an AuNR₁ outermost layer) the k_{et} decrease was more pronounced ($k_{et}=0.14 \times 10^{-7} \text{ cm} \times \text{s}^{-1}$) as compared to the previous AuNR₁ layer ($k_{et}=0.35 \times 10^{-5} \text{ cm} \times \text{s}^{-1}$, $n = 6$, table1) confirming the presence of very few gold nanorods within this last layer. The variation of the heterogeneous electron-transfer rate constants at the Au-(1,6HDT-AuNR₁)₄ multilayer modified electrode confirms the alternative electrochemical behaviour observed in the cyclic and square wave voltammograms depicted through peak shaped and plateau shaped CVs and SQWVs.

n	$k_{et} (\text{cm} \times \text{s}^{-1})$	self-assembly time (h)	$\beta (\text{\AA}^{-1})$	Tunnelling distance (\AA)
1	0.48×10^{-8}	14	0.92	17.04
2	1.63×10^{-5}	7		
3	0.62×10^{-7}	16	0.77	17.04
4	0.94×10^{-5}	10		
5	0.22×10^{-7}	19	0.83	17.04
6	0.35×10^{-5}	12		
7	0.20×10^{-7}	19	0.86	17.04
8	0.14×10^{-7}	15		

Table 1. Heterogeneous electron-transfer rate constants, k_{et} and tunnelling parameter, β , calculated for each self-assembled layer within the Au-(1,6HDT-AuNR₁)₄ multilayer, using the R_{CT} parameters obtained from the fittings of the EIS spectra (table 2) and based on equations (1)-(3).

The electron transfer process is switched on when the outermost layer is an AuNR₁ layer (high k_{et} , table 1, $n = 2, 4, 6$) and switched off when the outermost layer is a 1,6HDT layer (low k_{et} , table1, $n = 1, 3, 5, 7$). As the distance from the underlying bare gold electrode is increasing and the surface coverage with rods is decreases, the electron transfer process becomes slower (low k_{et} , table 1, $n = 8$, total film thickness: $188,85 \pm 1.05 \text{ nm}$). The tunnelling distance was estimated taking into consideration the length of the C-C, C-S and S-Au bonds which are 1.54\AA , 1.82\AA and respectively 2.85\AA (Jiang, J.; Lu, W. & Luo, Y., 2004). The variation of the tunnelling parameter, β , suggest that the electron tunnelling process is more efficient at the thiol layers self-assembled on the gold nanorods than at the 1,6HDT self-assembled on the bare gold electrode (lower values of β). Overall, the electron transfer process is faster at Au-(1,6 HDT-AuNR₁)₄ multilayer modified electrode than at bare gold electrode (up to $n = 6$) demonstrating a catalytic effect of the small rods as outermost layers. Electrochemical impedance spectroscopy (EIS) measurements were performed for each layer self-assembled on the gold electrodes. The Nyquist plots of the bare gold ($n = 0$) and Au-1,6HDT-SAM modified electrode ($n = 1$) are presented in Figure 6 whereas the Nyquist plots recorded at the Au-(1, 6HDT-AuNR₁)₄ multilayer modified electrode ($n = 2-8$) are presented

in Figure 7. The fittings of the EIS spectra were performed using the non-linear least square-fit procedure and the equivalent electrical circuits presented in Figure 8. Randles circuit was used for fittings of the bare gold EIS spectra ($n = 0$, Figure 6), whereas the other two equivalent electrical circuits were used for fittings of the EIS spectra of the film modified electrodes. The impedance responses varied with the type of layer self-assembled on the gold electrodes. The Warburg impedance for semi-infinite planar diffusion is the sum of concentration impedances which are linked to the mass transport (ionic diffusion) and to the kinetics of the charge transfer being given by the equation (4):

$$Z_d = \frac{\sigma}{\sqrt{\omega}} - \frac{i\sigma}{\sqrt{\omega}} \quad (4)$$

where

$$\sigma = \frac{RT}{n^2 F^2 A \sqrt{2}} \left\{ \frac{1}{c_R \sqrt{D_R}} - \frac{1}{c_O \sqrt{D_O}} \right\} \quad (5)$$

The parameters D_R and D_O represent the diffusion coefficients of the reduced and oxidized species ($1.76 \times 10^{-6} \text{ cm}^2 \text{ s}^{-1}$), c_R and c_O are the solution concentrations of the reduced and oxidized species ($c_R = c_O = 0.5 \times 10^{-3} \text{ mol/cm}^3$), σ is the mass transfer coefficient and ω is the angular frequency ($\omega = 2\pi f$, f is the alternative voltage signal frequency, Hz). The other parameters have the same meaning as previously mentioned. The total impedance at the bare gold electrode is described by the equation (6) and the Randles electrical circuit pictured in Figure 8a:

$$Z_a = R_s + \frac{R_{CT} + \sigma \omega^{-\frac{1}{2}} - i(2\sigma^2 C_{dl} + \omega C_{dl} R_{CT}^2 + 2\omega^{\frac{1}{2}} R_{CT} \sigma C_{dl} - \sigma \omega^{-\frac{1}{2}})}{(1 + \omega^{\frac{1}{2}} \sigma C_{dl})^2 + (\omega C_{dl} R_{CT} + \omega^{1/2} \sigma C_{dl})^2} \quad (6)$$

where R_s (Ω) is the solution resistance, R_{CT} (Ω) is the charge transfer resistance and C_{dl} (F) is the double layer capacitance. The Nyquist plots (Figure 6, $n = 1$) shows that the self-assembly of the 1,6hexanedithiol on bare gold electrode generates a very high resistance to the charge transfer (table 2), depicted through depressed semicircle for all range of frequencies with no evident diffusion profile at low frequencies. The 1,6hexanedithiol monolayer is changing the dielectric properties of the electrode surface generating a new film resistance R_f and film capacitance C_f . The total impedance at the Au-1,6HDT-SAM and Au-(1,6HDT-AuNR₁)₃ modified electrodes is given by the equation (7). The detailed expression of the real (Z'_b) and imaginary (Z''_b) complex impedances are presented in Appendix A, at the end of this chapter. The complex impedances were written by taking R_{CT} , R_f , as resistances, $1/i\omega C_{dl}$, $1/i\omega C_f$, as capacitances and applying Ohm's and Kirchhoff's laws to the connection of these elements in the electrical circuit. The parameter "i" is $\sqrt{-1}$.

$$Z_b = Z'_b + Z''_b \quad (7)$$

For a higher number of layers ($n = 7, 8$) the fittings of the EIS spectra were performed using the electrical circuit depicted in Figure 8c. The equation describing the total impedance Z_c , corresponding to this electrical circuit is presented in Appendix A. The electronic blocking effect induced by the 1,6hexanedithiol monolayer determined an increase of 3 orders

magnitude in the charge transfer resistance, R_{CT} ($n = 1$, table 2, Figure 6) as compared to the bare gold electrode ($n = 0$, table 2, Figure 6) and ~ 16 times decrease of C_{dl} demonstrating that the distance between the redox probes in solution and the underlying bare gold surface has increased.

This effect of the aliphatic chain thiol has been frequently observed at SAM modified electrodes (Chou et al., 2009; Su et al., 2006). The sequential self-assembly of the AuNR₁ layer has determined a decrease of the charge transfer resistance by 3 orders of magnitude ($n = 2$, table 2). The corresponding EIS spectrum featured a small semicircle at high and intermediate frequencies, which is due to the coupling between R_{CT} and C_{dl} parameters and a straight line at low frequencies (Figure 7a, $n = 2$, red circles) implying semi finite planar diffusion to the film (slope unity). The R_{CT} parameter relates to surface modifications that enhance/hinder the electron transfer process at the electrode/solution interface. The strong decrease of R_{CT} upon self-assembly of the AuNR₁ layer proves that these small rods (35.48 nm length per 14.52 nm width, Figure 1a and 1b) have a high catalytic activity for the $[\text{Fe}(\text{CN})_6]^{3-/4-}$ redox probes facilitating the electron transfer at the electrode/solution interface. Additionally, the strong decrease in film resistance, R_f , which is a tunnelling resistance in this case, proves that the gold nanorods assures a highly efficient electron tunnelling through the underlying 1,6HDT-SAM.

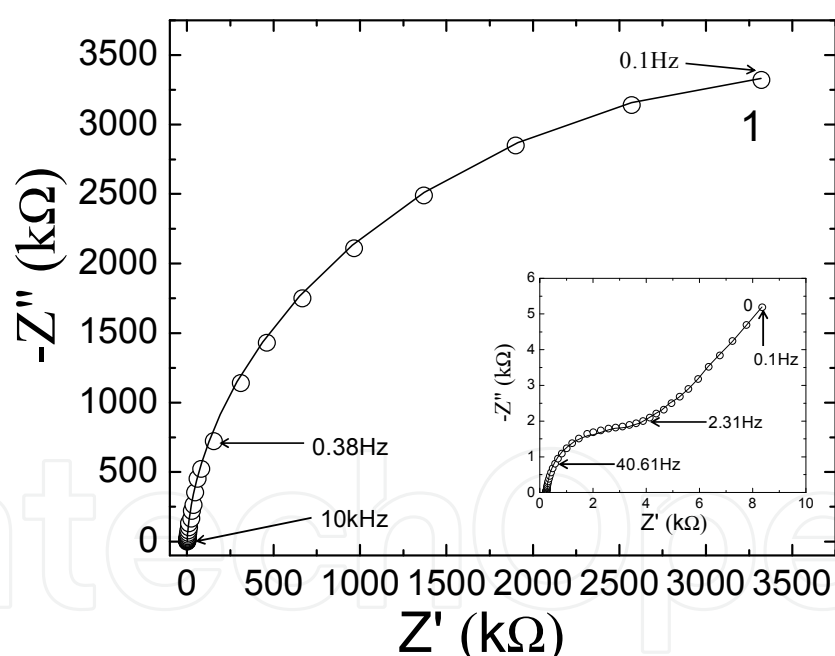


Fig. 6. Nyquist diagrams recorded at bare gold ($n = 0$) and Au-1,6HDT-SAM modified electrode ($n = 1$) in aqueous solution of 0.1M NaClO_4 and 0.0005M $[\text{Fe}(\text{CN})_6]^{3-/4-}$. The experimental data are represented by circles whereas the theoretical curves calculated using the parameters values in Table (2) are represented by lines.

The film capacitance, C_f , has slightly increased upon AuNR₁ self-assembly implying an increase of electrode area. Further build-up of the film on the gold electrodes, by the self-assembly of a third layer (1,6HDT) has determined a two orders magnitude increase in the charge transfer resistance ($n = 3$, table 2, Figure 7b, wine circles plot) as compared to the

previous AuNR₁ layer ($n = 2$, table 2, Figure 7a) demonstrating a hindered electron transfer process. It is interestingly to remark the fact that the 1,6hexanedithiol seems to have a weaker insulating effect when self-assembled on gold nanorods surface than on bulk gold. The decrease of C_{dl} for $n = 3$, (table 2) as compared to the C_{dl} of the previous layer ($n = 2$, table 2) demonstrates an increase of distance between the redox probes in solution and the underlying gold nanorod layer. This decrease of C_{dl} for the dithiol layers confirms the supposition that the cetyltrimethyl ammonium bromide stabilizing the rods will be removed during the self-assembly of the dithiol layers. Moreover, the consecutive increase of film resistance, R_f , and decrease of film capacitance, C_f , ($n = 3$, table 2) demonstrates that the electron tunnelling process is slow and the increase of area of the electrode is smaller at the 1,6HDT outermost layer. These alternating insulating/conductive features of the multilayer modified electrode are repeated through similar variation of the R_{CT} , C_{dl} , R_f , C_f parameters up to the 6 layers (table 2).

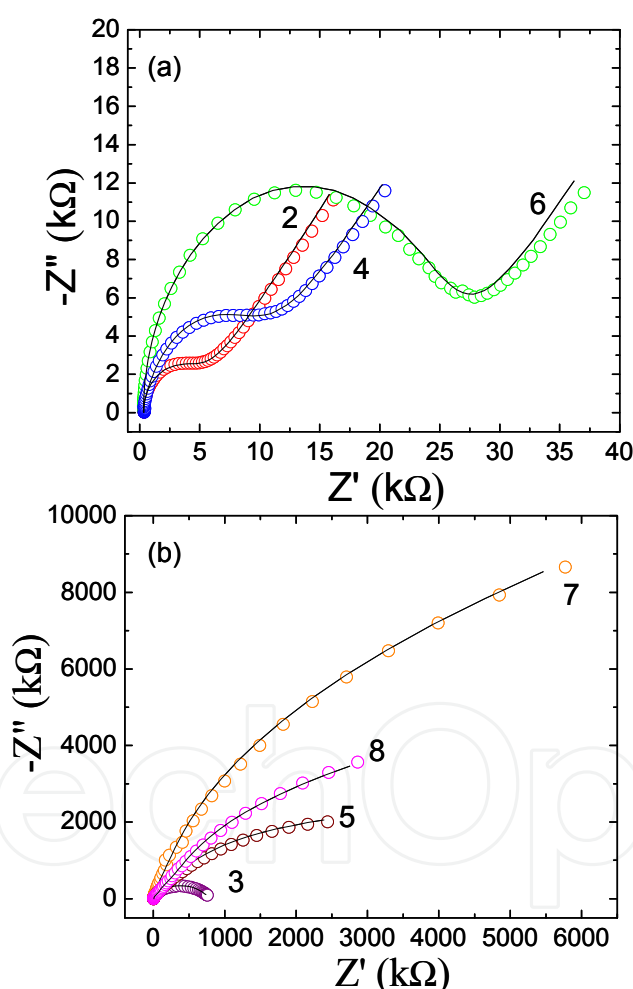


Fig. 7. Nyquist diagrams recorded at the Au-(1, 6HDT-AuNR₁)₄ multilayered modified gold electrodes in aqueous solution of 0.1M NaClO₄ and 0.0005M [Fe(CN)₆]^{3-/4-}: 1,6HDT outermost layers ($n = 3, 5, 7$) and AuNR₁ outermost layers ($n = 2, 4, 6, 8$), respectively.

The charge transfer resistance has drastically increased from 7th to the 8th layer self-assembled on the gold electrodes demonstrating that the last layer of gold nanorods has a low surface coverage with rods ($n = 7, 8$, table 2) and in consequence the electron transfer

process is slow. The C_{dl} has practically no variation passing from the 7th to the 8th layer proving that the main effect in the electrochemical process is caused by the 1,6HDT layer ($n = 7$, hindered electron transfer) than by the few rods from the 8th layer. Similarly, the capacitance of the film, C_f , is practically constant for the two last layers suggesting that area of the electrode has no variation upon self-assembly of the 8th layer (AuNR₁ layer). The film resistance has increased (compare R_f , $n = 7$ and R_f $n=8$) implying that some material is still attached to the substrates. The variation of these parameters confirms the pyramidal growth of the multilayered film on gold electrodes, as shown by AFM imaging (Figures 2, 3). The additional R'_f and C'_f parameters may suggest that the electron transfer process becomes very slow when the film thickness is too high. Overall, the variation of R_{CT} , C_{dl} , R_f , C_f parameters demonstrate that a maximum of 6 layers self-assembled on the gold electrodes is the optimal number of layers which assures a very efficient electron transfer through the small gold nanorods layers and efficient electron tunnelling through the dithiol layers in the electrochemistry of $[Fe(CN)_6]^{3-/4-}$ redox probes. Moreover, the overall electrochemical process is strongly dependent of the nature of the outermost layer. This dependence of the electrochemical process on the nature of the outermost layer has been observed for the first time at mercaptosuccinic stabilized gold nanoparticle (Au-MSA)/poly-Lysine multilayers self-assembled on gold electrodes (Chirea et al., 2005). The difference between these two types of multilayers is in the nature of the interaction between the redox probes in solution and the outermost layers. The depressed semicircles observed in the EIS spectra of the 1,6HDT outermost layers are due to the insulating properties of the aliphatic chain of the dithiol which is blocking the electronic communication between the redox probes in solution and the underlying bare gold electrodes (Chou et al., 2009; Su et al., 2006).

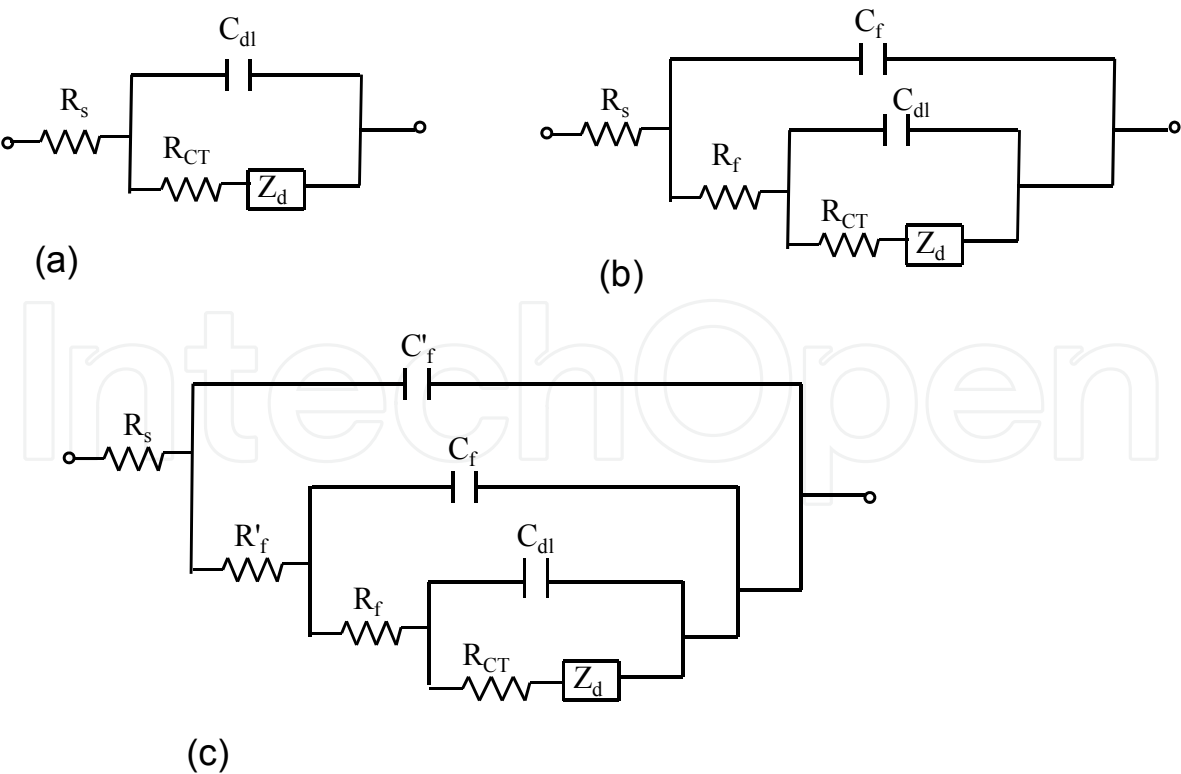


Fig. 8. Equivalent electrical circuits used for the fitting of impedance spectra represented in Figures 6, 7 and 10.

n	R_s (k Ω)	C_f (μ F)	R_f (k Ω)	C_f (μ F)	R_f (k Ω)	C_{dl} (μ F)	R_{CT} (k Ω)
0	0.292 (1.05)					0.83 (0.72)	2.61 (0.58)
1	1.20 (0.98)			0.14 (1.25)	2674 (0.28)	0.05 (0.35)	3510 (0.68)
2	0.297 (1.17)			0.97 (0.70)	3.58 (0.43)	2.48 (1.06)	1.03 (0.88)
3	1.24 (1.3)			0.13 (0.60)	430 (0.56)	0.18 (1.58)	269.3
4	0.303 (1.59)			0.43 (0.45)	19.87 (0.74)	1.56 (1.20)	1.78 (0.32)
5	1.73 (1.64)			0.07 (0.37)	2.60 (1.08)	0.03 (1.06)	772 (0.91)
6	0.34 (1.50)			1.57 (0.94)	4.38 (0.60)	1.77 (0.52)	4.82 (0.84)
7	2.14 (1.04)	0.16 (0.55)	2012 (1.2)	0.08 (1.16)	207.6 (0.54)	0.06 (0.38)	818.3 (0.55)
8	7.67 (1.20)	0.11 (0.51)	3306 (1.69)	0.07 (0.76)	324.5 (0.53)	0.08 (0.61)	1234 (0.73)

Table 2. Parameter values obtained from the fittings of the impedance spectra presented in Figures 6 and 7 using the nonlinear least-square fit. The percent errors from the fit for each element are given in parentheses.

In our previous work (Chirea et al., 2005), the depressed semicircles observed in the EIS spectra were due to a repelling effect (electrostatic repulsion) between the outermost layers of negatively charged gold nanoparticles (Au-MSA NPs) and negatively charge redox probes ($[Fe(CN)_6]^{3-/4-}$) in solution. It has to be mentioned also that the electron transfer was mediated by the Au-MSA NPs when they were covered by a positively charged poly-Lysine layer which facilitated the diffusion of the electroactive species through the film based on electrostatic attraction. In the case of the gold nanorod outermost layers, the diffusion of the electroactive species is favoured by the positively charged cetyltrimetyl ammonium bromide stabilizing the rods (proven by the diffusion profiles with slope unity at low frequencies in Figure 7a, $n=2, 4, 6$) whereas the electron transfer process is mediated by all the gold nanorods from a layer (proven by high Faradaic currents in the CVs and SQWV and decreased peak-to-peak separations, Figure 5a, c). The surface density of the rods is also decisive for the overall electrochemical process, an optimal surface coverage assuring a fast electron transfer (Chirea et al., 2010).

3.3.2 Electrochemical characterization of multilayers containing large gold nanorods

A different electrochemical behaviour was observed at the Au-(1,6HDT-AuNR₂)₄ modified electrodes. In this case, the size of the gold nanorods seems to have a high influence on the film growth and implicitly on the overall electron transfer process. Figure 9 shows the cyclic voltammograms (Figure 9a,b) and the square wave voltammograms (Figure 9c,d) recorded at the Au-(1,6HDT-AuNR₂)₄ multilayer modified gold electrodes in aqueous solution of 0.1M NaClO₄ and 0.0005M $[Fe(CN)_6]^{3-/4-}$. The average sizes of the rods incorporated into this film were 51.56 nm lengths per 14.80 nm width (AuNR₂, Figure 1d, e) with an aspect ratio of 3.48. Although these large rods were self-assembled in an end topography (vertically

aligned to the substrate surface) as the small rods, the film growth was different starting with the 4th layer self-assembled on the electrodes when the film density has increased upon the self-assembly of the AuNR₂ layer (compare Figure 3a and Figure 3b). The electrical properties of Au-1,6HDT-AuNR₂ multilayered modified electrodes were highly dependent on the type of outermost layer and the surface coverage with rods. As seen previously, the Faradic process was highly hindered by the 1,6hexanedithiol layers and this is proven by either a disappearance or a drastic decrease of peak currents in the CVs and SQWVs (Figure 9b, d, $n = 1, 3, 5, 7$). The electrochemistry of [Fe(CN)₆]^{3-/4-} redox probes was recovered upon the self-assembly of a AuNR₂ layers. For example, cyclic and square wave voltammograms with high peak currents and decreased peak separation were recorded at the Au-1,6HDT-AuNR₂ bilayer modified electrode ($n = 2$, Figure 9a,c red curve). The consecutive self-assembly of a 1,6HDT layer has diminished the Faradaic currents in the CVs and SQWVs ($n = 3$, Figure 9b, d, purple curve) which is equivalent to a hindered electron transfer process. The 4th layer self-assembled on the modified gold electrodes (an AuNR₂ layer) has restored the Faradaic currents in the CVs and SQWVs, but the electrochemical process seems to be slower than at the previous AuNR₂ outermost layer due to lower peak currents and higher peak to peak separation in the voltammograms (compare $n = 4$ and $n = 2$ in Figure 9a, c). The 5th layer self-assembled on the electrodes determined a complete blocking of the electronic communication between the [Fe(CN)₆]^{3-/4-} couple in solution and the underlying bare gold electrode ($n = 5$, Figure 9b,d wine curve). At the 6th layer (an AuNR₂ outermost layer) the electrochemical process is improved although it is even slower than at the previous AuNR₂ outermost layers (lowest Faradaic peaks and highest increase of peak-to-peak separations in the CVs and SQWVs, $n = 6$, Figure 9a, c). The last two layers bring no evident improvement of the electron transfer process at the 1,6HDT-AuNR₂ multilayer modified electrodes ($n = 7, 8$, Figure 9, orange and pink curves). At this stage of the multilayer build up, the surface coverage with rods is the lowest as compared to the previous AuNR₂ layers and the film density is the highest (Figure 3d). The Faradaic currents and the peak-to-peak separations in the CVs were: $I_a = 3.95\mu\text{A}$, $\Delta E_p = 0.071\text{V}$ for $n = 0$ (bare gold electrode), $I_a = 3.41\mu\text{A}$, $\Delta E_p = 0.100\text{V}$ for $n = 2$, (Au-1,6HDT-AuNR₂), $I_a = 0.33\mu\text{A}$ and $\Delta E_p = 0.368\text{V}$ for $n = 3$, (Au-1,6HDT-AuNR₂-1,6HDT), $I_a = 2.97\mu\text{A}$ and $\Delta E_p = 0.172\text{V}$ for $n = 4$, (Au-1,6HDT-AuNR₂)₂, $I_a = 2.61\mu\text{A}$ and $\Delta E_p = 0.244\text{V}$ for $n = 6$, (Au-1,6HDT-AuNR₂)₃ whereas for the other layers ($n = 1, 5, 7$ and 8) there were no peak currents in the CVs (Figure 9a,b). A more evident effect of each outermost layer self-assembled on the gold electrodes is proven by square wave voltammetry measurements which are showing a progressive decrease of Faradaic currents with increasing number of layers (Figure 9c,d) for both types of outermost layers. The peak currents and peak potential shifts were: $I_a = 9.40\mu\text{A}$ at 0.247V for $n = 0$, $I_a = 11.8\mu\text{A}$ at 0.232V for $n = 2$, $I_a = 0.180\mu\text{A}$ at 0.283V for $n = 3$, $I_a = 5.12\mu\text{A}$ at 0.246V for $n = 4$, $I_a = 0.107\mu\text{A}$ at 0.283V for $n = 5$, $I_a = 2.79\mu\text{A}$ at 0.286V for $n = 6$, $I_a = 0.084\mu\text{A}$ at 0.267V for $n = 7$ (Figure 9c and 9d).

The highest peak currents in the SQWVs were recorded at the Au-1,6HDT-AuNR₂ modified electrode ($n = 2$, Figure 9c) for which the electron transfer process is faster than at the bare gold electrode. A lower surface coverage of gold nanorods in the upper layers of the Au-(1,6HDT-AuNR₂)₄ film (Figure 3) determined a slightly slower electron transfer (lower peak currents in the CVs and SQWVs, $n = 4, 6, 8$, Figure 9c) than at the Au-1,6HDT-AuNR₂ bilayer modified electrode ($n = 2$, Figure 9c). The variation of the heterogeneous electron-transfer rate constants (table 3) estimated based on equation (1) –(3) and using the R_{CT} parameters obtained from the fittings of the EIS spectra (Figure 10, table 4) demonstrate that the electron

transfer process at the Au-(1,6HDT-AuNR₂)₄ modified electrodes is slower than at the at the Au-(1,6HDT-AuNR₁)₄ modified electrodes in the presence of the [Fe(CN)₆]^{3-/4-} redox couple. The heterogeneous electron-transfer rate constants estimated for the AuNR₂ outermost layers ($n = 2, 4, 6, 8$, table 3) are slightly lower than the heterogeneous electron-transfer rate constants estimated for the AuNR₁ outermost layers ($n = 2, 4, 6, 8$, table 1). This difference demonstrates a size effect of the gold nanorods, the short rods having a stronger catalytic activity toward the electrochemical process than the large rods. The k_{et} variations are consistent with previous published work in which was demonstrated a size effect of the rods for low and high surface coverages with rods at Au-1,6HDT-AuNR bilayers modified electrodes (Chirea et al. 2009, 2010). In those two reports was demonstrated for the first time the dependence of the electron transfer process on the size of these anisotropic gold nanorods and on the type of surface bonding (end or side surface bonding of rods). Other authors are starting to pursue similar studies. For example, it has been demonstrated a size effect toward electrochemistry of the same [Fe(CN)₆]^{3-/4-} couple at CdTe QD self-assembled on gold electrodes by means of mercaptoundecanoic acid and poly(diallyldimethylammonium chloride) (Kissling et al, 2010). The CdTe dots being very small (2.2nm, 2.5nm 2.9 nm) have slightly enhance mainly the reduction process. A size of 3nm or higher average diameters of the nanomaterials induces a higher enhancement of the electron transfer process as it was demonstrated in another report (Chirea et al., 2007).

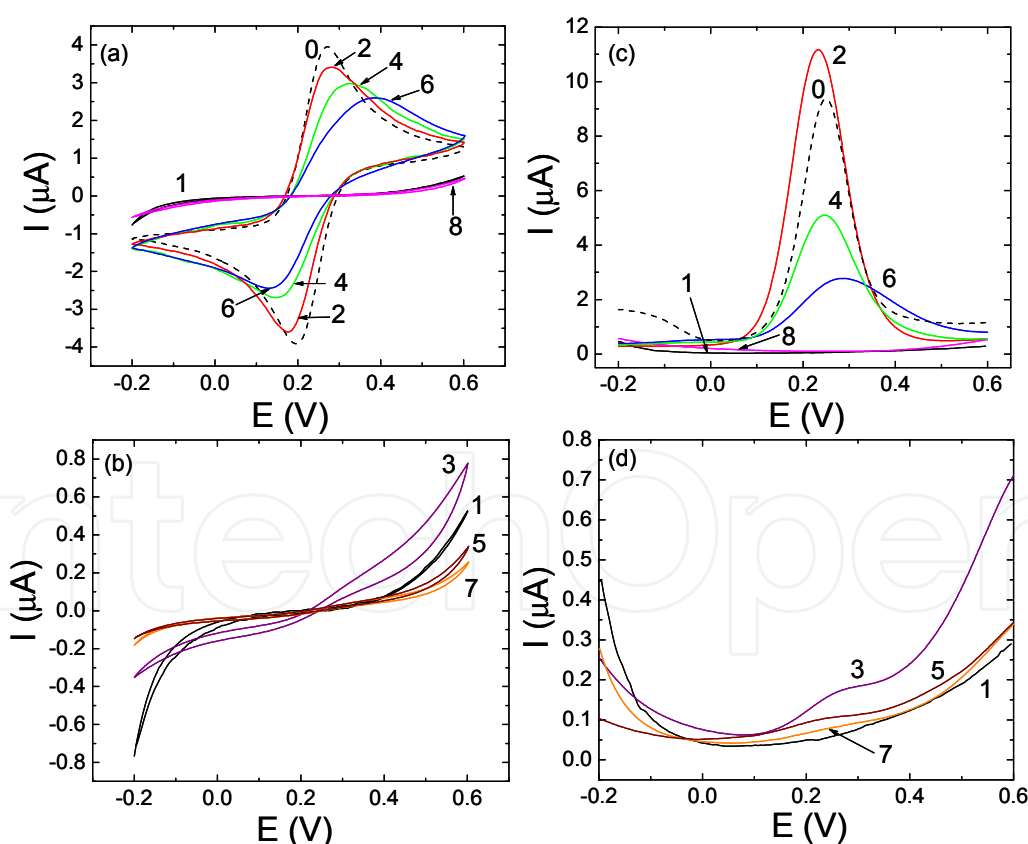


Fig. 9. Cyclic voltammograms (a, b) and square wave voltammograms (c, d) recorded at the Au-(1,6HDT-AuNR₂)₄ multilayered modified gold electrodes in aqueous solution of 0.1M NaClO₄ and 0.0005M [Fe(CN)₆]^{3-/4-}: bare gold ($n = 0$), 1,6HDT outermost layers ($n = 1, 3, 5, 7$) and AuNR₂ outermost layers ($n = 2, 4, 6, 8$), respectively.

n	$k_{et} (cm \times s^{-1})$	self-assembly time (h)	$\beta (\text{\AA}^{-1})$	Tunnelling distance (Å)
1	0.50×10^{-8}	14	0.91	17.04
2	1.02×10^{-5}	15		
3	0.25×10^{-7}	11	0.82	17.04
4	0.45×10^{-5}	16		
5	0.42×10^{-8}	18	0.92	17.04
6	0.15×10^{-5}	18		
7	0.30×10^{-8}	15	0.96	17.04
8	0.89×10^{-8}	6		

Table 3. Heterogeneous electron-transfer rate constants, k_{et} and tunnelling parameter, β , calculated for each self-assembled layer within the Au-(1,6HDT-AuNR₂)₄ multilayer, using the R_{CT} parameters obtained from the fittings of the EIS spectra (table 4) and based on equations (1)-(3).

The impedance responses recorded at the Au-(1,6HDT-AuNR₂)₄ multilayered modified electrodes in aqueous solution of [Fe(CN)₆]^{3-/4-} redox probes were dependent on the type of outermost layer (Figure 10). The EIS spectra featured depressed semicircles at 1,6HDT outermost layers (Figure 10b, $n=3, 5, 7$) for all range of frequencies. The charge transfer resistance R_{CT} has increased 3 or 2 orders of magnitude at the 1,6HDT outermost layers ($n=1, 5, 7$ and $n=3$, table 4) than at the bare gold electrode or AuNR₂ outermost modified electrodes ($n=2, 4, 6$, table 4). The C_{dl} varied with the insulating (decrease) or conductive properties (increase) of the outermost layers (table 4). Although, the charge transfer resistance R_{CT} has decreased at the AuNR₂ outermost layers, its tendency is to increase with increasing numbers of layers self-assembled on the gold electrodes implying that the electron tunnelling through the aliphatic chains of the dithiol and the electron transport mediated by the large gold nanorods is less efficient when the number of gold nanorods is decreasing due to the pyramidal growth of the film (Figure 3). The R_f has also a tendency to increase with increasing number of layers self-assembled on the electrodes being either 1,6HDT layers (higher R_f , $n=1, 3, 5, 7$, table 4) or AuNR₂ layers (lower R_f , $n=2, 4, 6, 8$, table 4).

The variation of these parameters demonstrates that the electron transfer is faster at the AuNR₂ outermost layers than at the 1,6HDT outermost layers and overall the increasing film thickness is affecting the overall electron transfer process. Interestingly, the additional parameters R'_f and C'_f have an evident effect on the overall electron transfer process starting the 3rd layer (table 4). These parameters are related to the electron tunnelling on a horizontal plane through the 1,6HDT layer connecting neighbours AuNR₂ (Scheme 1). As shown in the AFM images (Figure 4) these large rods can be covalently bonded on the horizontal plane, not only on a vertical plane. The increase of both film resistances R_f and R'_f and progressive decrease of the capacitances C_f and C'_f demonstrates that the efficiency of the electron tunnelling process is progressively diminished at low surface coverage with rods (in the upper layers) and the area of the electrodes is increasing. These electrochemical features do not imply that the Au-1,6HDT-AuNR₂ multilayers modified electrodes can be

less efficient for other electrochemical processes. For example, Chen-Zhong et al. have demonstrated that gold nanoparticles of 20-40 nm average diameters electrochemically deposited on gold electrodes and chemically modified by the self-assembly of thiolated DNA layers specific for anticancer drugs detection have determined a 20-40 fold increase of the detection limit (Chen-Zhong et al., 2005).

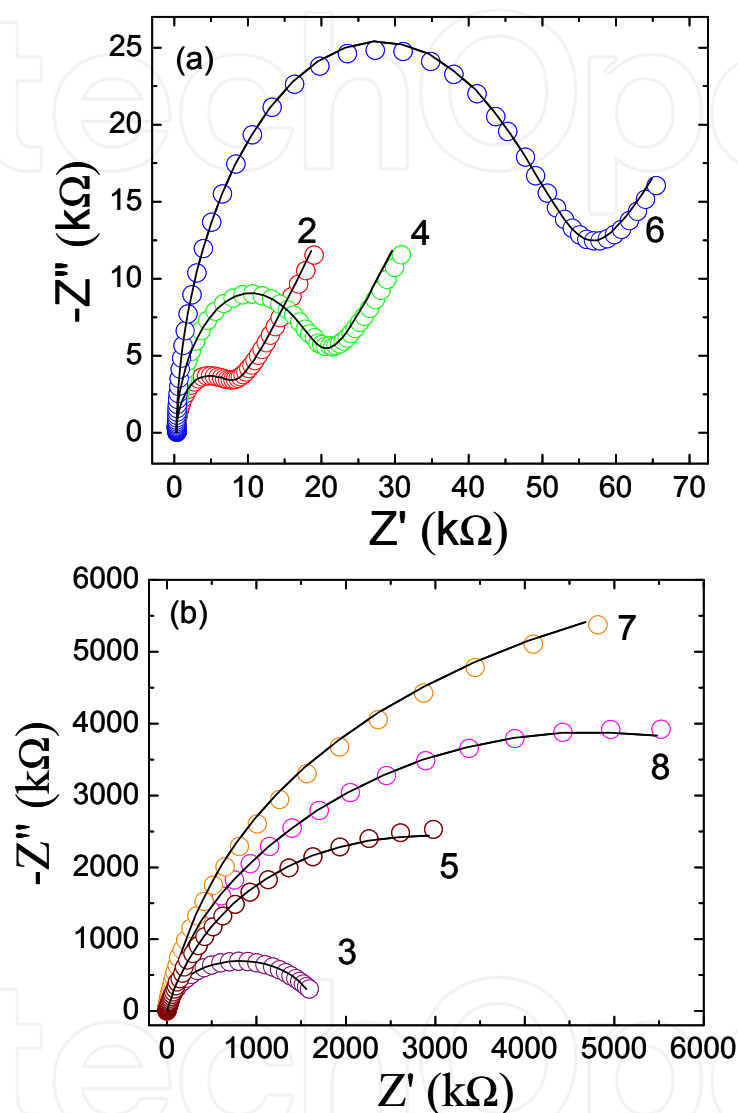


Fig. 10. Nyquist diagrams recorded at the Au-(1, 6HDT-AuNR₂)₄ multilayered modified gold electrodes in aqueous solution of 0.1M NaClO₄ and 0.0005M [Fe(CN)₆]^{3-/4-}: 1,6HDT outermost layers ($n = 3, 5, 7$) and AuNR₂ outermost layers ($n = 2, 4, 6, 8$), respectively.

Furthermore, recent studies have demonstrated that citrate stabilized gold nanoparticles embedded into poly-Lysine matrix through electropolymerization on glassy carbon electrodes from aqueous solution have improved the electron transfer kinetics of the [Fe(CN)₆]^{3-/4-} redox probes (Chirea et al., 2011a). Additionally, the citrate gold nanoparticles/poly-Lysine films were used for the electrostatic self-assembly of dsDNA. The resulted hybrid nanostructure has proven an improved sensitivity and a good detection limit for an anticancer drug, namely actinomycin D (Chirea et al., 2011b).

n	R_s (k Ω)	C'_f (μ F)	R'_f (k Ω)	C_f (μ F)	R_f (k Ω)	C_{dl} (μ F)	R_{CT} (k Ω)
0	0.290 (0.95)					0.78 (0.93)	2.53 (0.89)
1	1.05 (0.87)			0.18 (0.73)	2523 (0.62)	0.04 (0.67)	3427 (0.98)
2	0.290 (1.06)			0.90 (0.53)	5.53 (0.55)	1.79 (1.34)	1.64 (0.60)
3	1.44 (0.93)	0.81 (1.51)	274.7 (1.63)	0.10 (0.50)	625.6 (0.52)	0.05 (0.97)	682.4 (0.80)
4	0.296 (1.30)			0.58 (0.42)	14.65 (1.26)	1.43 (1.05)	3.75 (1.16)
5	4.77 (1.68)	0.17 (0.83)	2650 (0.83)	0.08 (0.83)	1330 (1.74)	0.03 (0.57)	3973.0 (0.91)
6	0.33 (1.18)			0.56 (0.32)	39.64 (1.16)	1.02 (1.36)	11.29 (0.65)
7	10.23 (0.95)			0.011 (0.69)	293 (0.63)	0.05 (0.65)	5558.3 (1.20)
8	7.07 (1.31)	0.014 (1.38)	2254 (1.32)	0.013 (0.82)	459 (0.98)	0.072 (0.61)	1899 (1.05)

Table 4. Parameter values obtained from the fittings of the impedance spectra represented in Figures 10 using the nonlinear least-square fit.

4. Conclusion

The dynamics of charge transfer at multilayered films composed of 1,6hexanedithiol/gold nanorods sequentially self-assembled on gold electrodes have been investigated as a function of the nature of the outermost layer and the size of the gold nanorods. The increase of R_{CT} upon covalent self-assembly of the 1,6hexanedithiol layers on bulk gold and gold nanorods layers is rationalized in terms of electronic blocking between the redox probes in solution and underlying gold nanorod layers or bare gold surface. The 3 orders magnitude decrease of R_{CT} upon consecutive covalent self-assembly of gold nanorods as outermost layers was rationalized in terms of increase in the interfacial concentration of the electroactive species at the gold nanorods surface (due to electrostatic attraction) , electron transport mediated by the rods and coherent electron tunnelling through the underlying 1,6hexanedithiol layers. The electron transfer process was faster (higher k_{et} values) at the multilayers containing short rods (35.48nm/14.52nm average sizes) than at the multilayers containing large rods (slightly lower k_{et} values, 51.56nm/14.80nm average sizes). An evident size effect, due to higher catalytic activity of the short rods, was observed in the electrochemical process. An optimal number of maximum 6 layers within the multilayered films have determined a fast electron transfer and coherent electron tunnelling at the hybrid nanostructured modified electrodes. The chemical structures of these films with an end bonding topography of the rods and their enhanced electrochemical properties make them very appealing for the fabrication of electronic devices or biosensors applications (Katz, E.&Willner , I., 2003).

5. Appendix A

The total impedance corresponding to the electrical circuit from Figure 8b, Z_b is written below:

$$Z_b = Z'_b + Z''_b$$
$$Z'_b = R_s + \frac{R_f + \sigma + R_{ct} + \frac{C_f R_{ct}^3 + C_f \sigma R_{ct}^2 + C_f R_{ct}^2 R_f - R_{ct}^2 R_f C_f - R_{ct}^3 C_f - R_{ct}^4}{C_{dl}^2 \omega^4} + \frac{2\sigma^2 + 2\sigma R_{ct} + 4\sigma R_f}{C_{dl}^2 \omega^{7/2}} + \frac{2R_f R_{ct}^2 + 2R_f C_f \sigma^3 + R_{ct}^3 + R_{ct}^2 \sigma}{C_{dl}^2 \omega^3} + \frac{4\sigma R_{ct} R_f + 2\sigma R_{ct}^2 + 2\sigma^2 R_{ct}}{C_{dl}^2 \omega^{5/2}} - \frac{2R_f C_f \sigma^3}{C_{dl}^2 \omega}$$
$$+ \frac{\left(C_f \omega R_f R_{ct}^2 + 2R_f C_f \omega \sigma^2 + 2\sigma R_{ct} R_f C_f \omega^{1/2} + \frac{2\sigma R_f C_f}{C_{dl} \omega^{1/2}} + \frac{R_{ct} C_f + R_f C_f + \sigma C_f}{C_{dl}^2 \omega} \right) + \left(\frac{C_f \sigma}{C_{dl}^2 \omega} + \frac{C_f R_{ct}^2}{C_{dl}} + \frac{C_f 2\sigma R_{ct}}{C_{dl}} + \frac{C_f 2\sigma^2}{C_{dl} \omega^{1/2}} + R_{ct}^2 + 2\left(\frac{\sigma}{\sqrt{\omega}}\right)^2 + 2\frac{\sigma R_{ct}}{\sqrt{\omega}} + \left(\frac{1}{C_{dl} \omega}\right)^2 + \frac{2\sigma}{C_{dl} \omega^{3/2}} \right)^2}{C_{dl} \omega^{3/2}}$$
$$+ \frac{-\frac{2R_f C_f \sigma^2 R_{ct}^2}{C_{dl}} + \frac{4C_f \sigma R_f R_{ct}^3 - 4\sigma R_f C_f R_{ct}^3 - 4\sigma^3 R_{ct} R_f C_f}{C_{dl} \omega^{1/2}} + R_f R_{ct}^4 + \frac{8\sigma^2 R_f R_{ct}^2}{\omega} + \frac{2\sigma R_f R_{ct}^3 + 2\sigma R_{ct}^2 R_f}{\omega^{1/2}} + \frac{4\sigma R_f C_f \sigma^3 R_{ct} + 4\sigma^2 C_f R_{ct} R_f - 4\sigma^3 R_{ct} R_f C_f}{C_{dl} \omega^{3/2}}}{C_{dl} \omega^{3/2}}$$
$$+ \frac{\left(C_f \omega R_f R_{ct}^2 + 2R_f C_f \omega \sigma^2 + 2\sigma R_{ct} R_f C_f \omega^{1/2} + \frac{2\sigma R_f C_f}{C_{dl} \omega^{1/2}} + \frac{R_{ct} C_f + R_f C_f + \sigma C_f}{C_{dl}^2 \omega} \right) + \left(\frac{C_f \sigma}{C_{dl}^2 \omega} + \frac{C_f R_{ct}^2}{C_{dl}} + \frac{C_f 2\sigma R_{ct}}{C_{dl}} + \frac{C_f 2\sigma^2}{C_{dl} \omega^{1/2}} + R_{ct}^2 + 2\left(\frac{\sigma}{\sqrt{\omega}}\right)^2 + 2\frac{\sigma R_{ct}}{\sqrt{\omega}} + \left(\frac{1}{C_{dl} \omega}\right)^2 + \frac{2\sigma}{C_{dl} \omega^{3/2}} \right)^2}{C_{dl} \omega^{3/2}}$$
$$+ \frac{\frac{2R_f C_f \sigma^2 R_{ct}^2}{C_{dl} \omega} - \frac{4\sigma^4 R_f C_f}{C_{dl} \omega} + \frac{4R_f C_f \sigma^4 + 4\sigma^2 R_{ct} R_f + 4\sigma^3 R_{ct} R_f}{\omega^2} + \frac{4R_f \sigma^4}{\omega^2} + \frac{8\sigma^3 R_{ct} R_f}{\omega^{3/2}} + \frac{8R_f \sigma^3}{C_{dl} \omega^{5/2}}}{\left(C_f \omega R_f R_{ct}^2 + 2R_f C_f \omega \sigma^2 + 2\sigma R_{ct} R_f C_f \omega^{1/2} + \frac{2\sigma R_f C_f}{C_{dl} \omega^{1/2}} + \frac{R_{ct} C_f + R_f C_f + \sigma C_f}{C_{dl}^2 \omega} \right) + \left(\frac{C_f \sigma}{C_{dl}^2 \omega} + \frac{C_f R_{ct}^2}{C_{dl}} + \frac{C_f 2\sigma R_{ct}}{C_{dl}} + \frac{C_f 2\sigma^2}{C_{dl} \omega^{1/2}} + R_{ct}^2 + 2\left(\frac{\sigma}{\sqrt{\omega}}\right)^2 + 2\frac{\sigma R_{ct}}{\sqrt{\omega}} + \left(\frac{1}{C_{dl} \omega}\right)^2 + \frac{2\sigma}{C_{dl} \omega^{3/2}} \right)^2}$$
$$Z''_b = -i \frac{R_f^2 C_f \omega R_{ct}^4 + 2R_f^2 R_{ct}^2 C_f \omega \sigma^2 + 4\sigma C_f \omega^{1/2} R_f^2 R_{ct}^3 + 6\sigma^2 C_f R_f^2 R_{ct}^2 + 4R_f^2 C_f \sigma^4 + 4\sigma^3 R_f^2 C_f \omega^{1/2} R_{ct} + \frac{4\sigma^3 R_{ct} R_f^2 C_f}{\omega^{1/2}}}{\left(C_f \omega R_f R_{ct}^2 + 2R_f C_f \omega \sigma^2 + 2\sigma R_{ct} R_f C_f \omega^{1/2} + \frac{2\sigma R_f C_f}{C_{dl} \omega^{1/2}} + \frac{R_{ct} C_f + R_f C_f + \sigma C_f}{C_{dl}^2 \omega} \right) + \left(\frac{C_f \sigma}{C_{dl}^2 \omega} + \frac{C_f R_{ct}^2}{C_{dl}} + \frac{C_f 2\sigma R_{ct}}{C_{dl}} + \frac{C_f 2\sigma^2}{C_{dl} \omega^{1/2}} + R_{ct}^2 + 2\left(\frac{\sigma}{\sqrt{\omega}}\right)^2 + 2\frac{\sigma R_{ct}}{\sqrt{\omega}} + \left(\frac{1}{C_{dl} \omega}\right)^2 + \frac{2\sigma}{C_{dl} \omega^{3/2}} \right)^2}$$
$$- i \frac{4\sigma R_f^2 C_f R_{ct}^2 + 4\sigma^3 R_f^2 C_f}{C_{dl} \omega^{1/2}} + \frac{8\sigma^2 R_f^2 C_f R_{ct} + R_{ct}^4}{C_{dl} \omega} + \frac{4\sigma^3 R_f^2 C_f + 4\sigma R_{ct}^3}{C_{dl} \omega^{3/2}} + \frac{8\sigma^2 R_{ct}^2}{C_{dl} \omega^2} + \frac{R_f R_{ct}^3 C_f + R_f^2 R_{ct}^2 C_f + \sigma R_f R_{ct}^2 C_f + C_f R_{ct}^4}{C_{dl}^2 \omega} + \frac{2\sigma^2 R_{ct} + 8C_f \sigma^3 R_{ct}}{C_{dl}^2 \omega^{5/2}} + \frac{\left(C_f \omega R_f R_{ct}^2 + 2R_f C_f \omega \sigma^2 + 2\sigma R_{ct} R_f C_f \omega^{1/2} + \frac{2\sigma R_f C_f}{C_{dl} \omega^{1/2}} + \frac{R_{ct} C_f + R_f C_f + \sigma C_f}{C_{dl}^2 \omega} \right) + \left(\frac{C_f \sigma}{C_{dl}^2 \omega} + \frac{C_f R_{ct}^2}{C_{dl}} + \frac{C_f 2\sigma R_{ct}}{C_{dl}} + \frac{C_f 2\sigma^2}{C_{dl} \omega^{1/2}} + R_{ct}^2 + 2\left(\frac{\sigma}{\sqrt{\omega}}\right)^2 + 2\frac{\sigma R_{ct}}{\sqrt{\omega}} + \left(\frac{1}{C_{dl} \omega}\right)^2 + \frac{2\sigma}{C_{dl} \omega^{3/2}} \right)^2}{C_{dl} \omega^{3/2}}$$

$$\begin{aligned} & \frac{2\sigma^2 R_f R_{ct} C_f + 6\sigma^2 R_f^2 C_f + 2\sigma^3 R_f C_f + C_f \omega R_f R_{ct}^3 + 2\sigma^2 R_{ct} R_f C_f \omega + 2\sigma R_{ct}^2 R_f C_f \omega^2 + \sigma C_f \omega R_f R_{ct}^2 + 2\sigma^3 R_f C_f \omega^2 + 2\sigma^2 R_{ct} R_f C_f \omega^2 + 2\sigma R_{ct}^2 R_f C_f \omega^2 + 2\sigma R_{ct} R_f^2 C_f \omega^2 + 2\sigma R_{ct}^2 R_f^2 C_f \omega^2 + 8C_f \sigma^2 R_{ct}^2}{C_{dl}^2 \omega^2} \\ & - i \frac{\left(C_f \omega R_f R_{ct}^2 + 2R_f C_f \omega \sigma^2 + 2\sigma R_{ct} R_f C_f \omega^{1/2} + \frac{2\sigma R_f C_f}{C_{dl} \omega^{1/2}} + \frac{R_{ct} C_f + R_f C_f + \sigma C_f}{C_{dl}^2 \omega} \right)^2 + \left(\frac{C_f \sigma}{C_{dl}^2 \omega} + \frac{C_f R_{ct}^2}{C_{dl}} + \frac{C_f 2\sigma R_{ct}}{C_{dl} \omega^{1/2}} + \frac{C_f 2\sigma^2}{C \omega} + R_{ct}^2 + 2 \left(\frac{\sigma}{\sqrt{\omega}} \right)^2 + 2 \frac{\sigma R_{ct}}{\sqrt{\omega}} + \left(\frac{1}{C_{dl} \omega} \right)^2 + \frac{2\sigma}{C_{dl} \omega^{3/2}} \right)^2}{\left(C_f \omega R_f R_{ct}^2 + 2R_f C_f \omega \sigma^2 + 2\sigma R_{ct} R_f C_f \omega^{1/2} + \frac{2\sigma R_f C_f}{C_{dl} \omega^{1/2}} + \frac{R_{ct} C_f + R_f C_f + \sigma C_f}{C_{dl}^2 \omega} \right)^2 + \left(\frac{C_f \sigma}{C_{dl}^2 \omega} + \frac{C_f R_{ct}^2}{C_{dl}} + \frac{C_f 2\sigma R_{ct}}{C_{dl} \omega^{1/2}} + \frac{C_f 2\sigma^2}{C \omega} + R_{ct}^2 + 2 \left(\frac{\sigma}{\sqrt{\omega}} \right)^2 + 2 \frac{\sigma R_{ct}}{\sqrt{\omega}} + \left(\frac{1}{C_{dl} \omega} \right)^2 + \frac{2\sigma}{C_{dl} \omega^{3/2}} \right)^2} \\ & - i \frac{\frac{2\sigma R_{ct} R_f^2 C_f + 2\sigma R_{ct}^2 R_f C_f + 2\sigma^2 C_f R_{ct} R_f + 4\sigma C_f R_{ct}^3}{C_{dl}^3 \omega^{3/2}} + \frac{2\sigma^3 + 4\sigma^2 R_{ct} + 4C_f \sigma^4}{C_{dl}^2 \omega^3} + \frac{2\sigma R_{ct} + 2\sigma R_{ct}^2 + 4\sigma^3}{C_{dl} \omega^{7/2}} + \frac{4\sigma R_f R_{ct} C_f + 4\sigma^2 R_f C_f + 4C_f \sigma^2 R_{ct}}{C_{dl}^3 \omega^{5/2}}}{\left(C_f \omega R_f R_{ct}^2 + 2R_f C_f \omega \sigma^2 + 2\sigma R_{ct} R_f C_f \omega^{1/2} + \frac{2\sigma R_f C_f}{C_{dl} \omega^{1/2}} + \frac{R_{ct} C_f + R_f C_f + \sigma C_f}{C_{dl}^2 \omega} \right)^2 + \left(\frac{C_f \sigma}{C_{dl}^2 \omega} + \frac{C_f R_{ct}^2}{C_{dl}} + \frac{C_f 2\sigma R_{ct}}{C_{dl} \omega^{1/2}} + \frac{C_f 2\sigma^2}{C \omega} + R_{ct}^2 + 2 \left(\frac{\sigma}{\sqrt{\omega}} \right)^2 + 2 \frac{\sigma R_{ct}}{\sqrt{\omega}} + \left(\frac{1}{C_{dl} \omega} \right)^2 + \frac{2\sigma}{C_{dl} \omega^{3/2}} \right)^2} \\ & - i \frac{\frac{2\sigma C_f R_{ct}^2}{C_{dl}^3 \omega^2} + \frac{R_{ct}^2 + 4\sigma^3 C_f}{C_{dl}^3 \omega^3} + \frac{2\sigma^2}{C_{dl}^3 \omega^{7/2}} + \frac{2\sigma^2}{C_{dl}^3 \omega^4} + \frac{2R_{ct} R_f C_f + R_f^2 C_f + 2\sigma R_{ct} C_f + 2\sigma^2 C_f + \sigma}{C_{dl}^4 \omega^3}}{\left(C_f \omega R_f R_{ct}^2 + 2R_f C_f \omega \sigma^2 + 2\sigma R_{ct} R_f C_f \omega^{1/2} + \frac{2\sigma R_f C_f}{C_{dl} \omega^{1/2}} + \frac{R_{ct} C_f + R_f C_f + \sigma C_f}{C_{dl}^2 \omega} \right)^2 + \left(\frac{C_f \sigma}{C_{dl}^2 \omega} + \frac{C_f R_{ct}^2}{C_{dl}} + \frac{C_f 2\sigma R_{ct}}{C_{dl} \omega^{1/2}} + \frac{C_f 2\sigma^2}{C \omega} + R_{ct}^2 + 2 \left(\frac{\sigma}{\sqrt{\omega}} \right)^2 + 2 \frac{\sigma R_{ct}}{\sqrt{\omega}} + \left(\frac{1}{C_{dl} \omega} \right)^2 + \frac{2\sigma}{C_{dl} \omega^{3/2}} \right)^2} \end{aligned}$$

The total impedance corresponding to the electrical circuit from Figure 8c, Z_c is given below:

$$Z_c = R_s + \frac{-iA}{C_f \omega} - \frac{i}{C_f \omega} \left(C_f \omega R_f R_{ct}^2 + 2R_f C_f \omega \sigma^2 + 2\sigma R_{ct} R_f C_f \omega^{1/2} + \frac{2\sigma R_f C_f}{C_{dl} \omega^{1/2}} + \frac{R_{ct} C_f + R_f C_f + \sigma C_f}{C_{dl}^2 \omega} \right)^2 + \frac{i}{C_f \omega} \left(\frac{C_f \sigma}{C_{dl}^2 \omega} + \frac{C_f R_{ct}^2}{C_{dl}} + \frac{C_f 2\sigma R_{ct}}{C_{dl} \omega^{1/2}} + \frac{C_f 2\sigma^2}{C \omega} + R_{ct}^2 + 2 \left(\frac{\sigma}{\sqrt{\omega}} \right)^2 + 2 \frac{\sigma R_{ct}}{\sqrt{\omega}} + \left(\frac{1}{C_{dl} \omega} \right)^2 + \frac{2\sigma}{C_{dl} \omega^{3/2}} \right)^2 + A$$

where

$$\begin{aligned}
 A = & \frac{R_f + \sigma + R_{ct}}{C_{dl}^4 \omega^4} + \frac{C_f R_{ct}^3 + C_f \sigma R_{ct}^2 + C_f R_{ct}^2 R_f - R_{ct}^3 C_f - R_{ct}^2 R_f C_f - R_{ct}^3 C_f - R_{ct}^4}{C_{dl}^3 \omega^2} + \frac{2\sigma^2 + 2\sigma R_{ct} + 4\sigma R_f}{C_{dl}^3 \omega^{7/2}} + \frac{2R_f R_{ct}^2 + 2R_f C_f \sigma^3 + R_{ct}^3 + R_{ct}^2 \sigma}{C_{dl}^2 \omega^3} + \frac{4\sigma R_{ct} R_f + 2\sigma R_{ct}^2 + 2\sigma^2 R_{ct}}{C_{dl}^2 \omega^{5/2}} - \frac{2R_f C_f \sigma^3}{C_{dl}^2 \omega} \\
 & + R_f' \left(\frac{C_f \omega R_f R_{ct}^2 + 2R_f C_f \omega \sigma^2 + 2\sigma R_{ct} R_f C_f \omega^{1/2} + \frac{2\sigma R_f C_f}{C_{dl} \omega^{1/2}} + \frac{R_{ct} C_f + R_f C_f + \sigma C_f}{C_{dl}^2 \omega} \right) + R_f' \left(\frac{C_f \sigma}{C_{dl}^2 \omega} + \frac{C_f R_{ct}^2}{C_{dl}} + \frac{C_f 2\sigma R_{ct}}{C_{dl} \omega^{1/2}} + \frac{C_f 2\sigma^2}{C_{dl} \omega} + R_{ct}^2 + 2 \left(\frac{\sigma}{\sqrt{\omega}} \right)^2 + \frac{\sigma R_{ct}}{\sqrt{\omega}} + \left(\frac{1}{C_{dl} \omega} \right)^2 + \frac{2\sigma}{C_{dl} \omega^{3/2}} \right) - \frac{2R_f C_f \sigma^2 R_{ct}^2}{C_{dl}} \\
 & + \frac{4C_f \sigma R_f R_{ct}^3 - 4\sigma R_f C_f R_{ct}^3 - 4\sigma^3 R_{ct} R_{ct}^3 - 4\sigma^3 R_{ct} R_f C_f}{C_{dl} \omega^{1/2}} + \frac{2R_f C_f \sigma^2 R_{ct}^2 - 4\sigma^4 R_{ct} R_f C_f}{C_{dl} \omega} + \frac{4R_f C_f \sigma^4 + 4\sigma^2 R_{ct} R_f + 4\sigma^3 R_{ct} R_f}{\omega^2} + \frac{8R_f \sigma^3}{\omega^{3/2}} + \frac{8R_f \sigma^3}{C_{dl} \omega^{5/2}} \\
 & - i \left(\frac{R_f^2 C_f \omega R_{ct}^4 + 2R_f^2 R_{ct}^2 C_f \omega \sigma^2 + 4\sigma C_f \omega^{1/2} R_f^2 R_{ct}^3 + 6\sigma^2 C_f R_f^2 R_{ct}^2 + 4R_f^2 C_f \sigma^4 + 4\sigma^3 R_f^2 C_f \omega^{1/2} R_{ct}}{\omega^{1/2}} + \frac{4\sigma^3 R_{ct} R_f^2 C_f}{\omega^{1/2}} + \frac{4\sigma R_f^2 C_f R_{ct}^2 + 4\sigma^3 R_f^2 C_f}{C_{dl} \omega^{1/2}} + \frac{8\sigma^2 R_f^2 C_f + 4\sigma R_{ct}^3}{C_{dl} \omega^{3/2}} + \frac{8\sigma^2 R_{ct}^2}{C_{dl} \omega^2} \right) \\
 & + \frac{8\sigma^3 R_{ct}}{C_{dl} \omega^{5/2}} + \frac{4\sigma^4}{C_{dl} \omega^3} + \frac{R_f R_{ct}^3 C_f + R_f^2 R_{ct}^2 C_f + \sigma R_f R_{ct}^2 C_f + C_f R_{ct}^4}{C_{dl}^2 \omega} + \frac{2\sigma^2 R_{ct} + 8C_f \sigma^3 R_{ct}}{C_{dl}^2 \omega^{5/2}} \\
 & + \frac{2\sigma^2 R_f R_{ct} C_f + 6\sigma^2 R_f^2 C_f + 2\sigma^3 R_f C_f + C_f \omega R_f R_{ct}^3 + 2\sigma^2 R_{ct} R_f C_f \omega + 2\sigma R_{ct}^2 R_f C_f \omega^2 + \sigma C_f \omega R_f R_{ct}^2 + 2\sigma^3 R_f C_f \omega + 2\sigma^2 R_{ct} R_f^2 C_f \omega^2 + 2\sigma R_{ct} R_f^2 C_f \omega^2 + \sigma R_{ct}^2 C_f \omega^2 + 8C_f \sigma^2 R_{ct}^2}{C_{dl}^2 \omega^2} \\
 & + \frac{2\sigma R_{ct} R_f^2 C_f + 2\sigma R_{ct}^2 R_f C_f + 2\sigma^2 C_f R_{ct} R_f + 4\sigma C_f R_{ct}^3}{C_{dl}^2 \omega^{3/2}} + \frac{2\sigma^3 + 4\sigma^2 R_{ct} + 4C_f \sigma^4}{C_{dl}^2 \omega^3} + \frac{2\sigma R_{ct} + 2\sigma R_{ct}^2 + 4\sigma^3}{C_{dl}^2 \omega^{5/2}} + \frac{4\sigma R_f^2 C_f + 4\sigma^2 R_f C_f + 4C_f \sigma^2 R_{ct}}{C_{dl} \omega^{5/2}} + \frac{2\sigma C_f R_{ct}^2}{C_{dl}^3 \omega^2} + \frac{R_{ct}^2 + 4\sigma^3 C_f}{C_{dl}^3 \omega^{7/2}} + \frac{2\sigma^2}{C_{dl}^3 \omega^4} \\
 & + \frac{2R_{ct} R_f C_f + R_f^2 C_f + R_{ct}^2 C_f + 2\sigma R_{ct} C_f + 2\sigma R_{ct}^2 C_f + 2\sigma^2 C_f + \sigma}{C_{dl}^4 \omega^3}
 \end{aligned}$$

6. Acknowledgment

Financial support from Fundação para a Ciência e a Tecnologia (FCT) of Portugal through the fellowship number SFRH/BPD/39294/2007 is gratefully acknowledged.

7. References

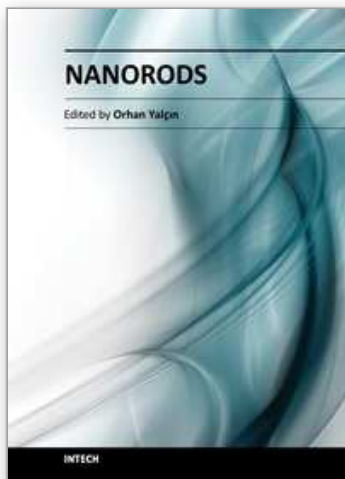
- Abdelrahman, A.I.; A.I.; Mohammad, A.M; Okajima, T.; Ohsaka, T. (2006). Fabrication and electrochemical application of three-dimensional gold nanoparticles: self-assembly., *J.Phys.Chem.B*, 2006, 110, pp.2798-2803, ISSN 1520-5207
- Bradbury, C.R.; Zhao, J.; Fermin, D.J. (2008). Distance-independent charge-transfer resistance at gold electrodes modified by thiol monolayers and metal nanoparticles. *J.Phys.Chem.C*, 2008, 112, pp.10153-10160, ISSN 1932-7455
- Chen, S.W.; Pei, R.J., (2001). Ion-induced rectification of the nanoparticle quantized capacitance charging in aqueous solution. *J.Am.Chem.Soc.* 2001, 123, pp.10607-10615, ISSN 1520-5126
- Chen-Zhong, L., Liu, Y., Luong, J.H.T. (2005). Impedance sensing of DNA binding drugs using gold substrates modified with gold nanoparticles. *Anal.Chem.*, 2005, 77, pp.478-485, ISSN 0003-2700
- Chirea, M.; Garcia-Morales, V.; Manzanares, J.A.; Pereira, C.; Gulaboski, R.; Silva, F. (2005) Electrochemical characterization of polyelectrolyte/gold nanoparticle multilayers self-assembled on gold electrodes. *J.Phys.Chem.B*, 2005, 109, pp.21808-21817, ISSN 1520-5207
- Chirea, M.; Pereira, C.M.; Silva, F. (2007). Catalytic effect of gold nanoparticles self-assembled into multilayered polyelectrolyte films, *J.Phys.Chem.C*, 2007, 111, pp.9255-9266, ISSN 1932-7455
- Chirea, M.; Cruz, A., Pereira, M.C., Silva, A.F., (2009). Size dependent electrochemical properties of gold nanorods. *J.Phys.Chem.C*, 2009, 113, pp.13077-13087, ISSN 1932-7455
- Chirea, M.; Borges, J Pereira, M.C., Silva, A.F., (2010). Density dependent electrochemical properties of vertically aligned gold nanorods. *J.Phys.Chem.C*, 2010, 114, pp.9478-9488, ISSN 1932-7455
- Chirea, M., Pereira, E.M., Pereira, C.M., Silva, F. (2011a). Synthesis of poly-Lysine/gold nanoparticles films and their electrocatalytic properties. *Biointerface Research in Applied Chemistry*, 2011, 1,(4) pp.119-126, ISSN 2069-5837
- Chirea, M., Pereira, E.M., Pereira, C.M., Silva, F. (2011b). DNA Biosensor for the Detection of Actinomycin D. *Biointerface Research in Applied Chemistry*, 2011, 1,(4), pp.151-159, ISSN 2069-5837
- Chou, A.; Eggers, P.K.; Paddon-Row, M.N.; Gooding, J.J. (2009). Self-assembled carbon nanotube electrode arrays: effect of length of the linker between nanotubes and electrode. *J.Phys.Chem.C*, 2009, 113, pp.3203-3211, ISSN 1932-7455
- Decher, G., Schlenoff, J. B., Eds. (2002). *Multilayer thin films: Sequentially assembly of nanocomposite materials*. Wiley-VCH: Weinheim, ISBN 9783527600571, Germany
- Feldheim, D.L. & Foss Jr, C. A. (2002). *Metal Nanoparticles: Synthesis, Characterization and Applications*, Marcel Dekker, Inc., ISBN 0-8247-0604-8. New York, 2002

- Finklea, H.O., Avery, S., Lynch, M., Furttsch, T. (1987). Blocking oriented monolayers of alkyl mercaptans on gold electrodes. *Langmuir* 1987,3,pp.409-413, ISSN: 1520-5827
- Finklea, H.O.(1996). In *Electroanalytical Chemistry: A Series of Advances*, A.J.Bard, I.Rubinstein, Eds. Marcel Dekker, Inc. New York, Basel, 1996, Vol.19, pp.110-318, ISBN 0-8247-4679-1
- Hicks, J.F.; Zamborini, F.P.;Murray, R.W.(2002).Dynamics of electron transfer between electrodes and monolayers of nanoparticles.*J.Phys.Chem.B.*,2002,106,pp.7751-7757,ISSN 1520-5207
- Horswell, S.L.; O'Neil, I.A.; Schiffrin, D.J.(2003).Kinetics of electron transfer at Pt nanostructured film electrode. *J.Phys.Chem.B.*,2003,107,pp.4844-4854, ISSN 1520-5207
- Jiang, J. Lu,W, Luo, Y .(2004). Length dependence of coherent electron transportation in metal-alkanedithiol-metal and metal-alkanemonothiol-metal junctions. *Chemical Physics Letters*, 2004, 400, pp 336-340, ISSN 0009-2614
- Kamat,P.V.(2008). Quantum Dot Solar Cells. Semiconductor nanocrystals as light harvesters, *J. Phys. Chem. C.*, 2008, 112,pp 18737-18753, ISSN1932-7455
- Katz,E.&Willner, I. (2003). Probing biomolecular interactions at conductive and semiconductive surfaces by impedance spectroscopy: routes to impedimetric immunosensors, DNA sensors and enzyme biosensors, *Electroanalysis*, 2003, 15, pp. 913-947, ISSN 1521-4109
- Katz,E. &Willner, I. (2004). Integrated Nanoparticle-Biomolecule Hybrid Systems: Synthesis, Properties and Applications, *Angew. Chem. Int. Ed.* (2004), 43, pp.6042 – 6108,ISSN 1521-3773
- Kissling, G.P.; Bünzly, C.; Fermin, D.J. (2010). Tuning electrochemical rectification via quantum dot assemblies.*J.Am.Chem.Soc.*,2010, 132, pp.16855-16861, ISSN 1520-5126
- Lasia, A.(1999).Electrochemical Impedance Spectroscopy and Its Applications. In *Modern Aspects of Electrochemistry*, Conway.B.E.; Bockris, J.; White, R.E., Edts., Kluwer Academic/Plenum Publishers, New York, 1999, 32, pp.143-248. URL: <http://www.chem.uw.edu.pl/studokt/wyklady/lasia/p1.pdf>
- Love, C.; Estroff, L.A; Kriebel,J.K.; Nuzzo,R.G.; Whitesides G. M. (2005).Self-assembled Monolayers of Thiolates on Metals as a Form of Nanotechnology, *Chem. Rev.*,2005,105,pp.1103-1169, ISSN 1520-6890
- Mirčeski, V.; Komorsky-Lovrić, S.; Lovrić, M.(2007). *Square wave voltammetry*. In :*Monographs in Electrochemistry*.F.Scholz (Ed.), Springer. 1st edition, 2007,Berlin, Germany, ISBN 978-3-642-09292-3.
- Nikoobakht, B. &El-Sayed ; M, A., (2003). Preparation and growth mechanism of gold nanorods using seed-mediated growth method, *Chem.Mater.*, 2003, 15,pp.1957-1962, ISSN 1520-5002
- Su, L.; Gao,F.; Mao, L.; (2006). Electrochemical properties of carbon nanotubes (CNT) film electrodes prepared by controllable adsorption of CNTs onto an alkanethiol monolayer self-assembled on gold electrodes, *Anal. Chem.*, 2006, 78,pp. 2651-2657, ISSN 0003-2700

- Xu., J.; Li, H. L.; Zhang, Y.(1993). Relationship between electronic tunnelling coefficient and electrode potential investigated using self-assembled alkanethiol monolayers on gold electrodes, *J. Phys. Chem.* 1993, 97, pp.11497-11500
- Yan, F., Sadik, O.A., (2001).Enzyme-modulated cleavage of dsDNA for studying interfacial biomolecular interactions. *J.Am.Chem.Soc.*,2001, 123, pp.11335-11340, ISSN 1520-5126

IntechOpen

IntechOpen



Nanorods

Edited by Dr. Orhan Yalçın

ISBN 978-953-51-0209-0

Hard cover, 250 pages

Publisher InTech

Published online 09, March, 2012

Published in print edition March, 2012

The book "Nanorods" is an overview of the fundamentals and applications of nanosciences and nanotechnologies. The methods described in this book are very powerful and have practical applications in the subjects of nanorods. The potential applications of nanorods are very attractive for bio-sensor, magneto-electronic, plasmonic state, nano-transistor, data storage media, etc. This book is of interest to both fundamental research such as the one conducted in Physics, Chemistry, Biology, Material Science, Medicine etc., and also to practicing scientists, students, researchers in applied material sciences and engineers.

How to reference

In order to correctly reference this scholarly work, feel free to copy and paste the following:

Mariana Chirea (2012). Charge Transfer Within Multilayered Films of Gold Nanorods, Nanorods, Dr. Orhan Yalçın (Ed.), ISBN: 978-953-51-0209-0, InTech, Available from:
<http://www.intechopen.com/books/nanorods/charge-transfer-within-multilayered-films-of-gold-nanorods>

INTECH
open science | open minds

InTech Europe

University Campus STeP Ri
Slavka Krautzeka 83/A
51000 Rijeka, Croatia
Phone: +385 (51) 770 447
Fax: +385 (51) 686 166
www.intechopen.com

InTech China

Unit 405, Office Block, Hotel Equatorial Shanghai
No.65, Yan An Road (West), Shanghai, 200040, China
中国上海市延安西路65号上海国际贵都大饭店办公楼405单元
Phone: +86-21-62489820
Fax: +86-21-62489821

© 2012 The Author(s). Licensee IntechOpen. This is an open access article distributed under the terms of the [Creative Commons Attribution 3.0 License](https://creativecommons.org/licenses/by/3.0/), which permits unrestricted use, distribution, and reproduction in any medium, provided the original work is properly cited.

IntechOpen

IntechOpen